Combustion and Flame 230 (2021) 111444

Contents lists available at ScienceDirect

Combustion and Flame

journal homepage: www.elsevier.com/locate/combustflame

A sectional soot formation kinetics scheme with a new model for coagulation efficiency

Zhijie Huo[a], Matthew J. Cleary[a,*], Mariano Sirignano[b], Assaad R. Masri[a]

[a] School of Aerospace, Mechanical and Mechatronic Engineering, The University of Sydney, NSW 2006 Australia
[b] Dipartimento di Ingegneria Chimica, dei Materiali e della Produzione Industriale, Università degli Studi di Napoli Federico II, Napoli, Italy

ARTICLE INFO

Article history:
Received 15 November 2020
Revised 29 March 2021
Accepted 31 March 2021
Available online 25 April 2021

Keywords:
Soot
Sectional method
Coagulation efficiency

ABSTRACT

A sectional scheme for soot formation is combined with a novel model for coagulation efficiency based on the thermal rebound concept and involves the minimisation of the Lennard-Jones potential energy between two colliding particles. Here, a novel generalisation of the interaction potential well depth is formulated for particles of any size or material composition that contains a free parameter λ which is related to the soot particle void fraction. A simplification that expresses the coagulation rate in an Arrhenius-like form is proposed so that the entire gas-phase and soot kinetics can be easily coupled and integrated using existing chemical kinetics solvers. The model is included in the sectional scheme, which accounts for nucleation, surface growth/oxidation, coagulation and fragmentation, and is validated against experimental data for a series of ethylene burner stabilised stagnation (BSS) premixed flames and a methane laminar coflow diffusion flame. The soot kinetics is discretised into lumped species according to soot particle size (or number of carbon atoms) and the soot evolution follows a 23-step abstract reaction scheme that is a reduced form of an existing multisectional soot kinetics scheme (Sirignano et al., Energy & Fuels 27, 2013). Overall, the model predictions produce a satisfactory agreement with the experimental data but there is considerable sensitivity to λ. In particular, λ has a strong effect on the soot particle size distribution (PSD) in the BSS flames. $\lambda = 1$ or 1.25 lead to an overprediction of large particle concentrations but result in the correct transition to a bimodal PSD as the stagnation plate separation distance increases, whereas $\lambda = 2$ is found to produce accurate predictions for nascent soot but suppresses the transition to a bimodal PSD. In the methane coflow diffusion flame increasing λ reduces the soot volume fraction but the predictions are also found to be very sensitive to the chosen numerical threshold for the lower soot size detection limit and results are presented for 2 nm and 7 nm thresholds for comparison against both laser-based and probe-based experimental data.

1. Introduction

Soot produced by combustion devices is a major source of atmospheric particulate matter which is hazardous, and especially harmful when inhaled into the human respiratory system. Regulations on soot emissions have progressively become more stringent necessitating further reductions in the emission of mass as well as the number of particles. To enable these improvements, soot models that are both accurate and computationally affordable are needed. Existing soot models include the method of moments (MOM) [1–4], the Monte Carlo method [5,6] and the sectional approach [7–10]. The method of moments and its variants are computationally efficient and solve transport equations for the moments of the particle size distribution (PSD). The equations include terms involving the unsolved higher-order moments so closure models are required. Closures based on logarithmic interpolation [2], direct quadrature [3] and hybrids of the two [4] can be found in the literature. The Monte Carlo methods are the most detailed and expensive of the CFD-based soot models, employing computational stochastic particles to solve the population balance equation (PBE) and predict the PSD in a probabilistic manner. Intermediate, in terms of detail and computational cost, the sectional approaches solve the PBE by direct discretisation of the PSD into sections or bins. In addition to discretisation according to soot particle size, other binning dimensions representing hydrogen to carbon (H/C) ratio [10–12], chemical reactivity [11,13,14] and particle morphology [10] can be added to enhance the detail of the modelling. These multisectional models have been tested against experimental data in small, laboratory-scale laminar flames [10,11,15–17] but, as the cost increases exponentially with the number of

* Corresponding author. .
E-mail address: m.cleary@sydney.edu.au (M.J. Cleary).

https://doi.org/10.1016/j.combustflame.2021.111444
0010-2180/

dimensions, they are computationally prohibitive for practical applications and sectional methods which discretise only on soot size are the most common.

Soot evolves through an interdependent sequence of processes that are typically categorised as nucleation, surface growth, coagulation/agglomeration, oxidation and fragmentation. It is widely accepted that polycyclic aromatic hydrocarbons (PAH) are the main gas precursors responsible for particle inception and PAH - PAH interaction is a key feature of models for soot nucleation [18–20]. The H-Abstraction-Acethylene-Addition (HACA) mechanism [21] is an important reaction path used to model the nucleation and surface growth [18,19]. Additionally, surface deposition via PAH - soot interactions is an important contributor to mass growth [22]. Coagulation and agglomeration refer to the collisions between soot particles leading to larger particles or aggregates. These are typically modelled as collision processes [23]. Oxidation leads to surface depletion and potentially fragmentation of larger soot particles into smaller particles [24,25]. Heterogeneous reactions between soot and gaseous oxidiser species such as O_2 and OH are included in many models [9,10,12,14,26]. With the exception of coagulation/agglomeration, these processes are the result of interactions between the solid soot phase and the gaseous molecular phase and models therefore need to have interphase coupling. Traditional PBE approaches require significant effort to account for phase change and coupling between the soot PSD and molecular species [8]. As discussed next, the soot kinetics methods offer a simpler alternative.

In the kinetic modelling form of the sectional approach, which is the focus of the present work, the soot bins can be thought of as *lumped species* (i.e. ensembles of real soot particles having similar physicochemical properties determined by size, hydrogen to carbon ratio, etc.) that are solved in the same computational scheme as the gas phase molecular species. Soot evolution clearly involves combinations of both physical and chemical processes that can be modelled in different forms independently [9,27], but the kinetic sectional model provides a mathematically and numerically elegant option by treating all of these as kinetic processes applied to each of the lumped soot species through abstract sectional reactions with Arrhenius-like rate models [10,12,13]. The lumped species (sections) are functionally like gas species and hence the interphase coupling is naturally achieved. In this way the gaseous chemistry and soot processes are implemented in a similar way and solved concurrently, and thus fully coupled, using the same kinetics solver.

Sectional methods for predicting soot evolution continue to develop [28–30]. One aspect of particular interest is the modelling of coagulation. The coagulation rate is typically modelled as the product of collision frequency and coagulation efficiency. While the collision frequency is quite well modelled already [23,31], there is not yet a consensus on modelling of the coagulation efficiency. This leads to inaccuracy in, for example, the ability to predict bimodal PSD distributions which result from a competition between rates of particle inception and coagulation [32]. Experimental evidence indicates that the coagulation efficiency for small soot particles can be several orders of magnitude smaller than that for larger soot particles, with non-linear increase to an efficiency of unity for particle diameters between 1 nm to 10 nm [33,34]. Singh et al. [35] and Eberle et al. [36] used different constant values for the coagulation efficiency. Zhang et al. [37] applied a step-shaped function which enforced low constant efficiency for small particles and constant unity efficiency for larger particles. Veshkini et al. [28] used the same model as Zhang et al. along with a reversible condensation efficiency model associated with PAH – PAH and PAH – soot interactions. Raj et al. [38] used an non-linear empirical fit to experimental data and Saggese et al. [12] proposed another empirical correlation between the coagulation efficiency and colliding particle size based on the experimental data reported in [33]. D'Alessio et al. [33] and Lindstedt et al. [9] proposed similar coagulation efficiency models which considered the thermal rebound effect [39]. Here, successful coagulation occurs when particles have insufficient thermal kinetic energy to escape the interaction potential well. These models have a physical basis but the potential well depth between colliding particles was unknown and the modelling was dependent on the value chosen for the Hamaker constant defined for Van der Waals interaction [40]. The Hamaker constant for benzene was suggested by D'Alessio et al. [33] and used in [15], but its value was tuned in other works to give best performance relative to data [9,16]. Elsewhere, linear interpolation of the Hamaker constant between upper and lower limits was employed to account for the impact of H/C ratio on the coagulation efficiency [10,11]. None of the aforementioned studies presented an explicit relationship between the interaction potential well depth and the Hamaker constant. The model of D'Alessio et al. [33] has an implied dependence of the potential well depth on the Lennard-Jones potential function, but explicit formulations showing the correlation to particle types and sizes was not presented.

In this study we propose a novel physics-based coagulation efficiency model combined with a sectional soot kinetics scheme that is discretised in particle size space. Each particle size bin is represented by one stable and one radical lumped species. The 23-step sectional scheme includes abstract reactions for nucleation, surface growth, coagulation, oxidation and fragmentation. It has been derived from the 33-step multisectional model reported in Sirignano et al. [10] which has dimensions for size, H/C ratio and particle morphology. The novelty of the coagulation efficiency model lies in the fact that the interaction potential well depth is explicitly formulated based on the Lennard-Jones potential and the resultant model has no direct dependence to the Hamaker constant. The expression for the potential well depth is quite general and is not restricted to any specific particle size or material composition. Although it has been derived independently and has a different mathematical form, our new model has conceptual similarities with the recently proposed model by Hou et al. [30]. However, that model overpredicts the coagulation efficiency by orders of magnitude compared to the experimental data from [33] and produces results very similar to the unity coagulation efficiency solutions. An additional goal of the current work is to present a solver-friendly version of the sectional scheme which can be directly coupled with a conventional gas-phase molecular chemical kinetics scheme. To achieve this, the coagulation rate, like all other processes described by the sectional scheme, is expressed in an Arrhenius-like form. The complete sectional soot kinetics model is validated through comparison to the experimental measurements of two laminar flames with different fuels and combustion mode; namely, an ethylene burner stabilised stagnation premixed flame [41] and a methane coflow diffusion flame [42,43].

The remainder of the paper is structured as follows. The model is presented in Section 2 with subparts for the sectional kinetics scheme, the coagulation model and a simplification of the coagulation model into an Arrhenius-like form. A comprehensive validation against experimental data appears in Section 3 and conclusions can be found in Section 4.

2. Models

2.1. Kinetics model

The gas-phase and soot kinetics are derived from the multisectional scheme presented in Sirignano et al. [10]. Essential details are given here for completeness and further information can be found in [10,15,16,44]. Readers who are familiar to this method may wish to go straight to Section 2.2.

Table 1
Sectional soot kinetics scheme.

			$K = A * T^n * EXP[-E/(R_{gas}T)] * (m * n_C)^k$				
		Reactions	A	n	E	k	m
Nucleation	Rx1	Ai + Aj = BINi	2.0e13	0.5	15,000	0	0
	Rx2	Aj + Aj = BINi	2.0e13	0.5	0	0	0
	Rx3	Ai + Ai = BINi	A_{coag}	n_{coag}	E_{coag}	0	0
Surface growth	Rx4	BINi = BINj + H	6.0e14	0	113,100	0.8	1
	Rx5	BINi + H = BINj + H2	3.54e13	0	16,000	0.467	1
	Rx6	BINi+ OH = BINj + H2O	3.54e13	0	4560	0.467	1
	Rx7	BINi($n_C \geq 19k$) + OH = BINj + H2O	8.85e13	0	4560	0.667	1
	Rx8	BINj + H = BINi	7.83e13	0	0	0	1
	Rx9	BINj + H2 = BINi + H	3.54e13	0	16,000	−1.1	1
	Rx10	Aj + BINj = BINi + H	8.0e12	0.5	0	0.59	0.35
	Rx11	Ai + BINj = BINi + H	2.0e13	0.5	15,000	0.59	0.35
	Rx12	Aj + BINi = BINi + H	2.0e13	0.5	15,000	0.59	0.35
	Rx13	Ai + BINi = BINi	A_{coag}	n_{coag}	E_{coag}	0	0
	Rx14	BINj + C2H2 = BINi + H	3e6	1.787	3262	0.616	1
	Rx15	BINj + C2H2 = BINi + H	3e0	1.787	3262	1.616	1
Coagulation	Rx16	BINj + BINj = BINi	8.0e12	0.5	0	0.35	1
	Rx17	BINi + BINj = BINi + H	2e13	0.5	15,000	0.35	1
	Rx18	BINi + BINi = BINi	A_{coag}	n_{coag}	E_{coag}	0	0
Oxidation	Rx19	BINi + OH = BINi + HCO	3.0e12	0.5	10,600	0.423	1
	Rx20	BINj + O2 = BINi + 2CO	4.3e11	0	8000	0.667	1
Fragmentation	Rx21	BINj + O2 = BINi + 2CO	8.6e7	0	8000	1.667	1
	Rx22	BINj($n_C \geq 19k$) + O2 = BINi + 2CO	4.3e-2	0	8000	1.667	1
	Rx23	BINj($n_C \geq 19k$) + O2 = BINi + 2CO	4.3e11	0	8000	−0.333	1

Unit: cal-K-cm-s
Ai is PAH, Aj is radicals; n_C is number of carbon
BINi is the stable lumped species, BINj is the corresponding radials.
A_{coag}, n_{coag} and E_{coag} are determined by the coagulation model.

The gas-phase reactions for pyrolysis and oxidation of hydrocarbon fuel are derived from [10] and are themselves based on the GRI-Mech 3.0 scheme for the C1 and C2 species [45] and the Miller and Melius mechanism for C3 and C4 species [46]. The sequential addition of acetylene molecules [21] is included, as well as the self-combination of resonantly stabilised radicals for the growth of PAH up to pyrene [47,48]. The soot kinetics is described by the 23 abstract reaction steps shown in Table 1. These reactions are abstract in the sense that they are applied to lumped species and the number of reactions depends on the discretisation that is chosen. *Ai* and *Aj* represent the stable and radical versions of the light PAH species: naphthalene (A2), acenaphthylene (A2R5), phenanthrene (A3) and pyrene (A4). The sectional soot species are denoted as *BIN* and the size discretisation is determined by the number of carbon atoms, n_C. The number of sections is denoted by N_S. The specific details of the discretisation including the size and n_C for each section are numerical considerations that are discussed in Section 3. The original multisectional scheme [10] has discretisation in size, H/C ratio and particle morphology spaces. To reduce computational cost, the H/C and particle morphology dimensions are removed here. The elimination of discretisation according to particle morphology removes any differentiation of large gaseous molecules, single particles, particle clusters and agglomerates. Hence, all the lumped species are treated as single particles in the present modelling. Furthermore, elimination of discretisation in H/C ratio space is compensated for by assigning this ratio for lumped species explicitly. In the past additional H atoms were prescribed to lumped so that the H/C ratio matched experimentally observed values [14–16]. However, reactions between lumped species must then release or compensate an abundance of hydrogen to conserve the mass of elemental hydrogen which is physically spurious and tends to be numerically unstable. Here, a more rigorous treatment has been proposed. Each size-dependent soot section is represented by two lumped species; a stable lumped species, BINi, that is assigned two hydrogen atoms, and a radical lumped species, BINj, that has one hydrogen atom.

The complete gas-soot mechanism consists 67 gaseous molecular species and $2 \times N_S$ sectional species. For $N_S = 20$, which is the base case setting in the present work, the kinetics scheme consists of 1358 reactions. As a comparison, multisectional soot schemes can have more than 450 species and more than 24,000 elementary reaction steps [49,50] or 900 lumped species and about 0.5 million reaction steps [10] and the associated computational cost is significantly higher than for the present scheme. The abstract reactions in Table 1 can be expanded into the complete sectional scheme by repetition of reactions looping over all PAHs, *Ai* and *Aj*, and sectional soot species, BINi and BINj. Here, i and j are not indexes, rather they represent stable and radical species, respectively. Hence, Ai is a general symbol for the stable PAH species: A2, A2R5, A3 and A4; while Aj is for the PAH radicals: A2*, A2R5*, A3* and A4*. Similarly, BINi and BINj are the general symbols representing the stable and radical lumped species, respectively. A product lumped species that falls between two bins is split between them. For example, the nucleation reaction Rx1 for pyrene, *A4*, and its radical, denoted as *A4*∗, is interpreted as

$$A4 + A4* = x\ \text{BINi-01} + y\ \text{BINi-02} + 8\ H_2, \tag{1}$$

and reaction Rx16 for BINj-07 (i.e. radical lumped species for section 7) and BINj-03 (i.e. radical lumped species for Section 3) leads to

$$\text{BINj-07} + \text{BINj-03} = x\ \text{BINi-07} + y\ \text{BINi-08}. \tag{2}$$

In each example the parameters x and y are found through conservation of both the number of carbon atoms and the number density of soot particles (i.e. $x + y = 1$). The released hydrogen in the first example ensures that H atoms are also conserved. Splitting lumped species between adjacent fixed nodes in the sectional scheme leads to some artificial broadening of the PSD. This effect is quantified in the Supplementary Material for the case of pure surface reactions. The broadened PSD has an approximately log-normal distribution around the exact solution and its standard

deviation correctly decreases with increasing number of soot sections.

The reaction steps in Table 1 model the five main soot evolution processes:

Nucleation: Rx1–Rx3 are for the conversion of light PAH's into the first soot sections. All forms of interaction are included, i.e. PAH - (PAH radical), (PAH radical) - (PAH radical) and PAH–PAH. Based on an assumed structural similarity [11], the rate coefficients for Rx1 and Rx2 are given by the coefficients for reactions of phenyl + benzene [51] and phenyl + phenyl [52], respectively, with scaling relative to n_C. The dimerisation of stable PAH molecules by Rx3 is modelled as a coagulation process with the rate coefficients determined according to the coagulation model presented below.

Surface growth: Once the first BIN is formed from PAH, the further evolution of the soot begins by formation of radicals BINj in Rx4, which models spontaneous H loss, and Rx5, Rx6 and Rx7 which model H-abstraction due to heterogeneous reactions between BINi and H and OH. The naphthalene reaction rate [14] is taken as a reference as explained in [11] and in this reduced scheme, the reaction rate parameters have been adjusted to account for the effect of hydrogen availability so that the scaling parameter k is reduced by 0.2 in Rx4 - Rx6 and Rx19 compared to [11]. Note that Rx7 is applied to BINs with $n_C \geq 19k$ to increase the rate of the H-abstraction pathway represented by Rx6 for larger particle sizes only. Rx8 and Rx9 are the backwards reactions of Rx4 and Rx5, respectively, acting as termination reactions for BIN radicals [16].

All forms of PAH addition to particles are considered; namely (PAH radical) - (BIN radical) in Rx10, PAH - (BIN radical) in Rx11, (PAH radical) - BIN in Rx12 and PAH - BIN in Rx13. The rate constants are determined in a way analogous to the nucleation reactions (Rx1 - Rx3) with scaling based on the number of carbons. Rx13 can be viewed as condensation of PAH onto particle surfaces and it is modelled using the coagulation rate presented below. The acetylene addition reactions (Rx14 and Rx15) combined with H-abstraction constitute the H-Abstraction-Acetylene-Addition (HACA) mechanism which tends to close aromatic rings forming peri-condensed aromatic compounds (PCAH) [19,21]. Rx15 accounts for increased rate of C_2H_2 addition with higher surface area of aggregates. The HACA reaction rate constants are based on the reaction rate of naphthyl + acetylene scaled by increasing collision frequencies [14,21].

Coagulation: Combination of soot particles into larger particles is modelled by (BIN radical) - (BIN radical) in Rx16 and BIN - (BIN radical) in Rx17, as well as by coagulation of two stable lumped species in Rx18. In Rx16 stable biphenyl-like compounds are formed and further growth is stalled until they are once again activated via Rx4 - Rx7. Rx17 models the formation of σ-bond connected aromatic molecules, also named oligomers of aromatic hydrocarbons (OAH), which can then develop into peri-condensed structures by hydrogen loss (Rx5) [11]. An analogy to phenyl + benzene [51] and phenyl + phenyl [52] is used for the rate constants for Rx16 and Rx17 with scaling by n_C. The coagulation rate in Rx18 is modelled as a pure physical process by forming larger lumped species upon collision of stable BIN species. Generally, coagulation itself does not alter directly the total soot volume fraction or soot mass but contributes significantly to the temporal evolution of the soot PSD [53]. As soot particle shape is not considered in the current work, there is no further consideration on the formation of fractal aggregates.

Oxidation: Hydroxyl radical (OH) is the dominant species responsible for soot oxidation [24] and is used to oxidise stable lumped species through Rx19 [16]. Oxidation of stable lumped species by O_2 is also modelled by Rx20 with the rate coefficients based on the reaction of naphthyl + O_2 [54].

Fragmentation: Reactions Rx21 - Rx23 are special oxidation processes to model fragmentation due to carbon removal from weak connecting sites in soot particles. Each of the fragmentation reactions represents different concepts [10]. Single particle fragmentation (Rx21) is induced by internal burning, whereas aggregate breakup into smaller aggregates (Rx22) or smaller single particles (Rx23) is induced by oxidation occurring around the soot agglomerate connection points. Note that Rx22 and Rx23 apply only to larger lumped radical species. The rate parameters are the optimal values given in Sirignano et al. [10] from comparison to experimentally measured particle size distributions [25]. In all fragmentation processes, the larger particles/aggregates split into two equal-sized particles/aggregates.

2.2. Coagulation model

The coagulation rate is modelled as $k = \beta\gamma$, where β is the collision frequency and $\gamma \in [0, 1]$ is the collision efficiency. Note that coagulation in this study refers only to physical combinations of stable (i.e. electrically neutral) lumped species. All particles are assumed to be spherical in the modelling presented here. Results for an alternative model in which particles larger than a certain threshold size are non-spherical with an empirical and constant fractal dimension are presented in the supplementary material available with the online version of this paper. The results using both the spherical and non-spherical assumption are very similar with only minor sensitivity around the valley of the bimodal PSD. However, the flexibility of the current model to include particle morphology is demonstrated and optimum fractal description can be used in different cases in practice. The model for collision frequency depends on the regime of the collision events. In the free molecular regime the collision frequency is modelled by analogy with the kinetic theory of gases in which colliding particles are treated as elastic hard spheres [23,31],

$$\beta_{i,j}^{f} = \left(\frac{\pi k_B T}{2}\right)^{1/2} \left(\frac{1}{m_i} + \frac{1}{m_j}\right)^{1/2} (d_i + d_j)^2, \tag{3}$$

where $k_B = 1.380649 \times 10^{-23} J/K$ is the Boltzmann constant, T is the temperature, m_i and m_j are the mass of particles, and d_i and d_j are the collision diameters of particles.

For particles in the continuum regime, collisions are the result of Brownian motion and the collision frequency is modelled by [23,31]

$$\beta_{i,j}^{c} = C \frac{2k_B T}{3\mu} \left(\frac{1}{d_i} + \frac{1}{d_j}\right)(d_i + d_j), \tag{4}$$

where μ is the dynamic viscosity of the fluid environment and C is the Cunningham correction factor for the Brownian particle diffusivities [55,56],

$$C = 1 + Kn\left(1.257 + 0.4e^{(-1.1/Kn)}\right), \tag{5}$$

with the Knudsen number, $Kn = \lambda_f / L$, where λ_f is the gas mean free path and L is the representative length scale, i.e. particle radius. In the simulations the regime is not identified directly and the collision frequency is modelled by the minimum of the free molecular and continuum values,

$$\beta = min(\beta_{i,j}^{f}, \beta_{i,j}^{c}), \tag{6}$$

which is essentially a model for the collision frequency in the transition regime. Various other approximations for the transition regime are available in the literature and a detailed comparison of some of them can be found in Otto et al. [57]. Generally, among the models the one based on the minimum given in Eq. (6) produces an upper bound for β and the model based on the harmonic mean of the two values produces a lower bound, with up to a

factor of two difference between these upper and lower bounds. Despite these differences in β our numerical tests with both the minimum and harmonic mean approximations produce essentially identical results for the soot particle size distribution as shown in the supplementary material. This finding may be case dependent and caution should be applied in selecting the most appropriate coagulation frequency model for specific conditions.

Following [33] the coagulation efficiency is modelled using the concept of thermal rebound [39] which assumes that a colliding particle rebounds elastically if its thermal velocity is sufficient to escape from the interaction potential well. Particles that do not escape are assumed to subsequently equilibrate in the potential well, resulting in a successful coagulation. Therefore a physical but simple approach is to model the coagulation efficiency as the probability of a particle having thermal kinetic energy smaller than the potential well depth. Assuming that the thermal velocity follows a Maxwell-Boltzmann distribution, and equating the thermal kinetic energy to the potential well depth leads to [33,58]

$$\gamma = 1 - \left(1 + \frac{\Phi_0}{k_B T}\right) exp\left(-\frac{\Phi_0}{k_B T}\right), \tag{7}$$

where Φ_0 is the depth of the interaction potential well (i.e. interaction potential energy minimum).

The total interaction potential energy between two clusters, that are each composed of primary molecular particles, can be approximated as the integral of the potential energy between every molecule in one cluster and the molecules in the other cluster. Based on this, Hamaker [40] formulated an expression for the Van der Waals attraction between spherical particles. Narsimhan et al. [59] added to this by accounting for the repulsive effect as particle separation approaches zero, and that approximation, which is limited to equal size particles, is now widely used for modelling the interaction potential energy between neutral atoms and molecules. Previous soot research [10,33] has used these ideas to model Φ_0, but the dependency on particle size and composition was not explicitly included and the models cannot be easily generalised. Here, we now extend this further by developing a more general expression for the interaction potential energy between two spherical soot particles of arbitrary size and material composition.

We start by considering two molecules, A and B, which, in general, are dissimilar although the following derivation is also valid when A and B are the same. The interaction potential energy between these molecules when the centres are separated by a distance r_{AB} can be approximated by the Lennard-Jones (LJ) potential function,

$$\Phi_{AB}(r_{AB}) = -\Phi_{AB,0}\left[\left(\frac{r_{AB,0}}{r}\right)^{12} - 2\left(\frac{r_{AB,0}}{r}\right)^{6}\right], \tag{8}$$

where $\Phi_{AB,0}$ is the potential well depth (potential minimum) and $r_{AB,0}$ is the centre-to-centre distance between A and B at which the potential reaches that minimum value. For pairs of relatively simple molecules of the same type, the LJ parameters (i.e. $\Phi_{AA,0}$, $r_{AA,0}$, $\Phi_{BB,0}$ and $r_{BB,0}$) can be obtained from experimental measurements or numerical calculations [60]. For two dissimilar molecules the parameters can then be approximated through combining rules [61],

$$\Phi_{AB,0}\ \sigma_{AB,0}^{6} = \left(\Phi_{AA,0}\ \sigma_{AA,0}^{6}\ \Phi_{BB,0}\ \sigma_{BB,0}^{6}\right)^{1/2}$$
$$\Phi_{AB,0}\ \sigma_{AB,0}^{12} = \left[\frac{(\Phi_{AA,0}\ \sigma_{AA,0}^{12})^{1/13} + (\Phi_{BB,0}\ \sigma_{BB,0}^{12})^{1/13}}{2}\right]^{13}, \tag{9}$$

where $\sigma_{AA,0} = r_{AA,0}/(2^{1/6})$.

The interaction potential concept is now extended to clusters of molecules (i.e. particles). Consider two spherical particles, p_1 and p_2, whose radii are R_1 and R_2, and which each have uniform material composition with p_1 containing q_1 molecules of A per unit volume and p_2 containing q_2 molecules of B per unit volume with

$$q_i = \frac{1}{\lambda\ V_{M,i}} \tag{10}$$

where the index $i \in [1,2]$ and V_M is the volume of a single molecule. $\lambda = 1/p_f$ is a model parameter that represents the reciprocal of the molecular packing fraction, $p_f = 1 - \nu_f$, where ν_f is the void fraction. It is taken here as a constant but sensitivity to its value is discussed in detail below. Following Hamaker [40], the LJ potential function for the interaction between p_1 and p_2 separated by distance r_{12} is given by the integral

$$\Phi_{12}(r_{12}) = \int_{\nu_1} q_1 d\nu_1 \int_{\nu_2} q_2 \Phi_{AB}(r_{AB}) d\nu_2. \tag{11}$$

Substitution of Eq. (8) then gives

$$\begin{aligned}\Phi_{12}(r_{12}) = {} & \frac{\Phi_{AB,0}\pi^2 q_1 q_2}{r_{12}} \times \\ & \left\{ \frac{r_{AB,0}^{12}}{360}\left[-\frac{1}{105(r_{12}+R_1+R_2)^5} - \frac{R_1+R_2}{21(r_{12}+R_1+R_2)^6} - \frac{2R_1R_2}{7(r_{12}+R_1+R_2)^7} \right.\right. \\ & + \frac{1}{105(r_{12}-R_1+R_2)^5} - \frac{R_1-R_2}{21(r_{12}-R_1+R_2)^6} - \frac{2R_1R_2}{7(r_{12}-R_1+R_2)^7} \\ & + \frac{1}{105(r_{12}+R_1-R_2)^5} + \frac{R_1-R_2}{21(r_{12}+R_1-R_2)^6} - \frac{2R_1R_2}{7(r_{12}+R_1-R_2)^7} \\ & \left. - \frac{1}{105(r_{12}-R_1-R_2)^5} + \frac{R_1+R_2}{21(r_{12}-R_1-R_2)^6} - \frac{2R_1R_2}{7(r_{12}-R_1-R_2)^7} \right] \\ & + \frac{r_{12}r_{AB,0}^6}{3}\left[ln\frac{r_{12}^2-(R_1+R_2)^2}{r_{12}^2-(R_1-R_2)^2} + \frac{2R_1R_2}{r_{12}^2-(R_1+R_2)^2} + \frac{2R_1R_2}{r_{12}^2-(R_1-R_2)^2} \right] \left.\right\}. \end{aligned} \tag{12}$$

Importantly, upon setting $R_1 = R_2$ in Eq. (12) the potential function reduces to the formulation derived for equal-sized particles in Narsimhan et al. [59]. The potential well depth for the coagulating particles, p_1 and p_2, is given by the minimum of Eq. (12) with respect to r_{12}. As this function has only one minimum, the value can be easily found numerically

$$\Phi_0 = min(\Phi_{12}), \tag{13}$$

The usefulness of the above novel coagulation efficiency model hinges on finding suitable values for the LJ parameters $\Phi_{AB,0}$ and $r_{AB,0}$ which are composition dependent. Soot particles are complex combinations of various hydrocarbons and simplification is needed here. Soot particles with high hydrogen content are formed mainly by oligomers of aromatic hydrocarbons whose steric conformation is known to hinder coagulation, while particles with low hydrogen content tend to be formed by intrinsically planar pericondensed aromatic compounds (PCAH) which readily form parallel stacks [10,62,63]. Previous work [10,64,65] used the H/C ratio to assist in the modelling of these structural differences with H/C = 0 and H/C = 1 (or higher) determining upper and lower limits for the coagulation rate of soot particles with the same number of carbon atoms. Following a similar line, we now examine the effects of using the LJ parameters for carbon-carbon (C-C), benzene-benzene (A1-A1) and pyrene-pyrene (A4-A4) pairings to approximate the H/C = 0 limit, H/C = 1 limit and an intermediate ratio of H/C = 0.625, respectively. The relevant parameters are summarised in Table 2.

The predicted coagulation efficiency for two equal-sized particles with diameter $D = 2R_1 = 2R_2$ is shown in Fig. 1 which also includes results for the coagulation efficiency obtained from atomic force microscopy experimental data for thermophoretically collected soot in premixed ethylene flames [33] and from the model suggested by Raj et al. [38] for use in their Monte Carlo simulations that was extracted from correlations of measured and computed soot mass spectra. Quantitative uncertainties exist in both sets of comparison data but they act as useful reference points against which a preliminary assessment of our new model can be

Table 2
LJ parameters for three simple coagulation pairings.

	$\Phi_m(J)$	$r_m(m)$	$V_{molecule}(m^3)$
C-C [66]	9.853e-22	3.70e-10	20.58e-30[a]
A1-A1 [67]	2.291e-20	3.77e-10	147.6e-30[b]
A4-A4 [67]	8.916e-20	3.67e-10	264.4e-30[c]

[a] computed by van der Waals radius [68].
[b] measured by the x-ray diffraction ionisation method [69].
[c] computed by density of pyrene.

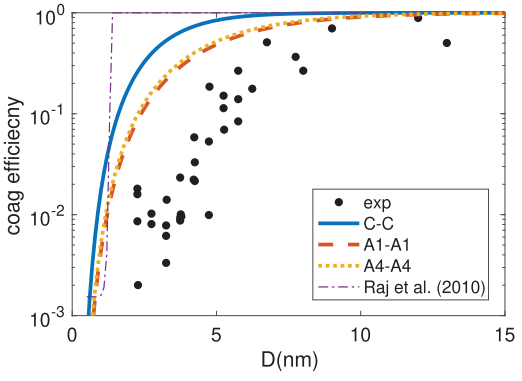

(a) $\lambda = 1$

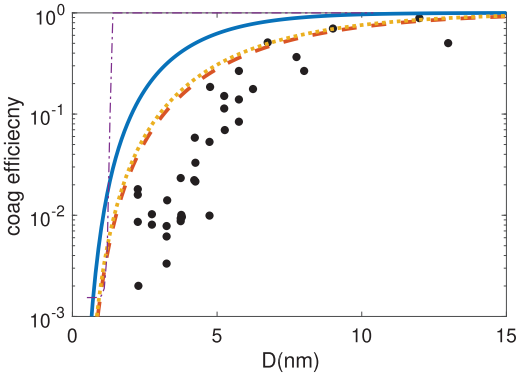

(b) $\lambda = 1.25$

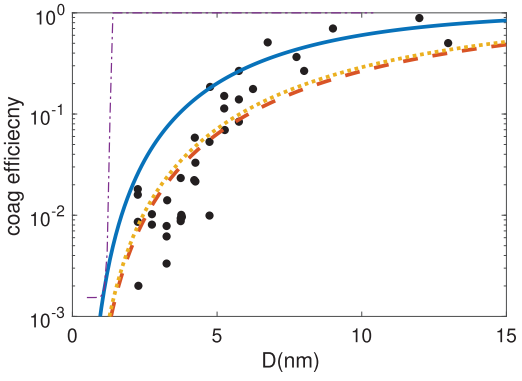

(c) $\lambda = 2$

Fig. 1. Coagulation efficiency versus particle diameter for the coagulation of two equal sized particles. Model results are presented for different material combinations and λ. Experimental results are from [33] and the Raj et al. model is from [38].

made. The predictions are for fixed $T = 1500$ K and for three values of λ between 1 and 2. The coagulation efficiency for these conditions increases non-linearly by about three orders of magnitude for soot particles in the size range 1 nm $< D <$ 10 nm. Generally, the new model predicts coagulation efficiency similar to those by of Raj et al.'s model for particles smaller than 1.5 nm. Experimental data is not available in this small size range. As the particle size increases, the new model shows better agreement with the experimental data and gives a smooth transition to a coagulation efficiency of one. As expected, the model based on LJ parameters for C-C coagulation produces the highest coagulation efficiency, while modelling using the LJ parameters for A1-A1 coagulation gives the lowest values. Intermediate coagulation efficiencies, although much closer to A1-A1 than C-C, are produced when the LJ parameters for pyrene-pyrene coagulation are used. The model results also show a trend of decreasing coagulation efficiency with increasing λ. Higher values of λ correspond to larger particle void fractions and thus smaller q (i.e. fewer molecules per unit volume). Recalling Eq. (12), such conditions lead to a smaller value of the interaction potential well depth leading to greater probability of colliding particles escaping the attractive forces and lower coagulation efficiency. Overall, the best agreement with the experimental data occurs for $\lambda = 2$, especially for the larger particles for which experimental data is expected to be more accurate. Here, the curves for LJ parameters for C-C an A1-A1 envelope the scattered data quite well. Uncertainty remains around the best value to use for the LJ parameters. In two-dimensional sectional methods where the H/C ratio is explicitly considered [10] different parameters could be chosen for different H/C values but in the one dimensional sectional method used here the differentiation is not possible. In the flame modelling below, due to the relatively high hydrogen content of PAHs, the A1-A1 parameters will be used for calculating the coagulation efficiency for the dimerisation reactions (Rx3). For sectional soot lumped species coagulation (Rx18) the LJ parameters for C-C are used. For the PAH - BIN condensation reactions (Rx13) LJ parameters for C-A1 pairings are used with help from the combining rule, Eq. (9).

2.3. Simplified Arrhenius-like coagulation model

Most of the reactions in the sectional soot scheme presented in Table 1 are in an Arrhenius form with the pre-exponential factor expanded to $A(m \times n_C)^k$, while the exponent and activation energy are conventional. The exceptions are the reactions involving coagulation; Rx3, Rx13 and Rx18. To facilitate use of exiting chemical kinetics interpreters and solvers, it is convenient to further manipulate the coagulation model so that it to fits within an Arrhenius-like rate formulation.

According to Eq. (6) the collision frequency, β, is given by the minimum of the values obtained by the free molecular and continuum models. Inspection of this minimum over a temperature range of 300 K to 2200 K (typical in hydrocarbon flames) reveals that β scales quite closely with $T^{0.5}$. This leads to a similar exponential form extensively used in soot kinetics modelling, e.g. the work by D'Anna and Kent [15], Blacha et al. [70] and Saggese et al. [71]. The coagulation rate coefficient can therefore be manipulated into an Arrhenius-like form, viz.

$$\begin{aligned} k_{coag} &= \beta\gamma \\ &\approx A_\beta\ T^{0.5}\ A_\gamma\ T^{n_\gamma}\ exp[-E_\gamma/(R_{gas}T)] \\ &\approx (A_\beta A_\gamma)\ T^{0.5+n_\gamma}\ exp[-E_\gamma/(R_{gas}T)]. \end{aligned} \tag{14}$$

The coagulation rate parameters listed in Table 1 are then

$$A_{coag} = A_\beta A_\gamma,$$
$$n_{coag} = 0.5 + n_\gamma,$$

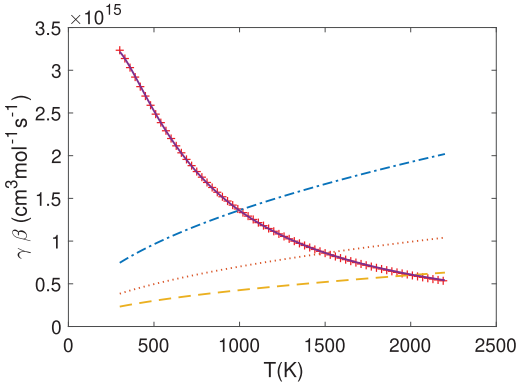

(a) BIN10 - BIN1

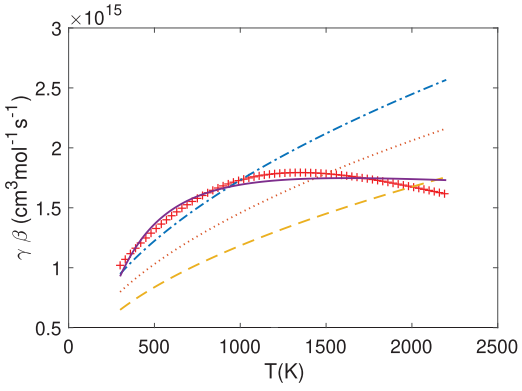

(b) BIN10 - BIN6

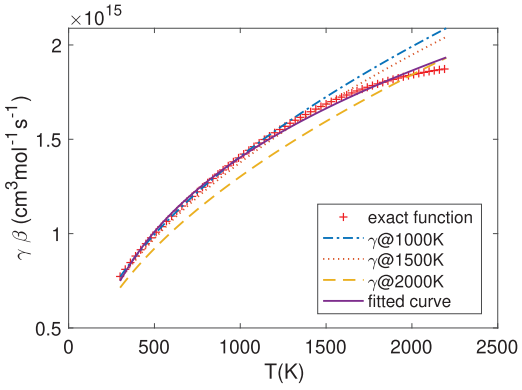

(c) BIN10 - BIN10

Fig. 2. Coagulation rate constants versus temperature for three different bin size combinations. Fitted results are for the Arrhenius-like simplification. Exact results are for the unsimplified model presented in Section 2.2. Fixed temperature results are for the exact model with the coagulation efficiency calculated for the indicated temperature values.

$$E_{coag} = E_{\gamma}. \tag{15}$$

Here $A_{\beta} = \beta/T^{0.5}$ and A_{γ}, n_{γ} and E_{γ} are different for each coagulation reaction and are obtained in a pre-processing operation by nonlinear least-squares fitting against the original model formulation over the 300–2200 K temperature range.

Figure 2 shows coagulation rates versus temperature for three different coagulation types involving a range of bin sizes. The fitted results using the simplified formulation are compared against the exact results from the model presented in Section 2.2. Generally there is a very good match between these. Figure 2a shows a typical trend for the coagulation rate of small particles which decreases as the temperature rises, while Figure 2c shows the opposite trend which is typical for larger particles with coagulation efficiency very close to unity. For particles of intermediate size shown in Fig. 2b, the coagulation rate increases first with increasing temperature and then at higher temperatures a decreasing trend is evident. This is mainly caused by a change in the dominance of either collision frequency, β, or coagulation efficiency, γ. For small and large particles one of these two parameters is dominant and the coagulation rate trend is monotonic. For intermediate sizes, neither parameter is dominant and the non-monotonic trend is produced. As points of comparison to illustrate the importance of temperature on γ, coagulation rate curves with γ calculated using three different fixed temperature values are also shown in Fig. 2. Note that the other temperature dependencies in the coagulation model remain unfixed. Other simple temperature independent coagulation efficiency models are reported elsewhere [12,38]. The higher that fixed temperature value is, the lower the coagulation rate. Fixing the temperature in calculating γ leads to the wrong trend in coagulation rate for small to intermediate sized particles. For larger particles this trend error is not observed because γ approaches unity and is not significantly affected by temperature. In addition to the good agreement to the exact model equations, it is shown in the Supplementary Material that the simplified exponential form of the coagulation rate correctly attains a self-similar size distribution during pure coagulation.

Table 3
Discretisation in particle size space.

BIN	n_C	D (nm)	BIN	n_C	D (nm)
1	24	0.80	11	48,965	10.16
2	48	1.00	12	127,308	13.91
3	96	1.27	13	343,732	19.37
4	192	1.60	14	962,448	27.30
5	384	2.01	15	2,791,100	38.93
6	768	2.53	16	8,373,301	56.15
7	1613	3.24	17	25,957,232	81.87
8	3548	4.21	18	83,063,141	120.64
9	8161	5.56	19	274,108,366	179.61
10	19,586	7.45	20	931,968,443	270.08

3. Validation against experimental data

3.1. General information

Two different flame configurations are calculated and further details are reported in Sections 3.2 and 3.3. General aspects about the computational implementation are provided here while some specific details, e.g. CFD grid and boundary conditions, are discussed as needed in those subsequent sections.

The combined gas-phase and sectional soot kinetics scheme is tested using the OpenSMOKE++ solvers [72,73] which are compatible with the OpenFOAM libraries [74]. In all simulations, thermodynamic and transport properties for gas-phase species are from the Chemkin compatible databases of Smith et al. [45] and Kee et al. [66], respectively. On the assumption that soot particles are formed by PAH [10], the thermodynamic properties of lumped species are the same as for pyrene per unit mass. The transport property data from Richter et al. [14] is used for both the PAH and the lumped species.

The soot PSD is discretised into 20 sections (bins) based on the number of carbon atoms ranging from $n_C = 24$ to $n_C = 10^{10}$ as shown in Table 3. Soot particles are assumed to have a constant bulk density of 1.8 g/cm^3. The density does not vary with λ although that refinement of the model is possible in principle. The sections span a diameter range of 0.8 nm $\leq D \leq$ 270 nm. The

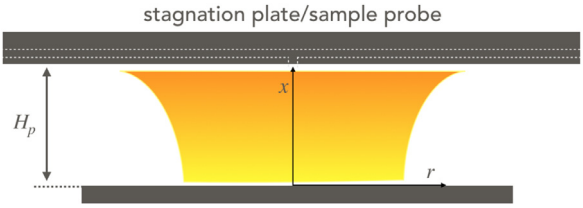

Fig. 3. Schematic representation of a BSS flame and illustration of stagnation plate and coordinate system.

resolution, which is refined at the smaller end and expands greatly at the larger end, is comparable to what is used in Richter et al. [14], D'Anna et al. [15] and Saggese et al. [12]. To ensure numerical convergence, additional simulations of the ethylene BSS premixed flames using 10, 40 and 80 sections are presented in the supplementary material available with the online version of this paper. While the modelling with 10 bins is obviously too coarse, showing relatively large numerical error compared to the converged results and the experimental data, the 20 bin results are quite close to the results for 40 and 80 bins. The computational cost with varying number of bins is also analysed in the supplementary material. Compared to the cost of computing the 20 bin case, the 40 bin simulations are around three times more expensive, while the 80 bin simulations are more expensive by a factor of between 8 and 12.

In the present work sensitivity to variations in porosity, and hence λ, are analysed through simulations with three different values of porosity (i.e. 0, 0.2 and 0.5) corresponding to $\lambda = 1$, 1.25 and 2, respectively, that are commensurate with the range of experimentally observed porosity values reported in the literature. For example, Song et al. [75] measured porosity of 0.26 in carbon black using an Hg porosimeter. Ghiassi et al. [76] analysed high-resolution transmission electron microscopy (HR-TEM) images of soot particles and estimated the porosity to be 0.41 ± 0.03. In the study of soot oxidation and fragmentation, Neoh et al. [24] found the porosity to be as high as 0.7 which seems to be an upper limit amongst the values reported elsewhere.

3.2. Ethylene BSS premixed flames

3.2.1. Case setup

The burner stabilised stagnation (BSS) flame that is shown in Fig. 3 involves a flame impinging on a flat stagnation plate [41]. To minimise interference the sampling probe is located at a small orifice in the centre of the plate from where the soot PSD is analysed by a scanning mobility particle sizer. The plate height above the burner is H_p. Here we model flame cases in which the jet issues a premixture of 16.3% ethylene, 23.7% oxygen and 60% argon by volume (equivalence ratio $\phi = 2.07$) into the surroundings with an equivalent cold gas velocity of 8 cm/s.

A series of BSS flames with varying H_p is simulated with a single coordinate in the x-direction. The 1D OpenSMOKE++ solver was previously used for the BSS flames with a different soot model in [12,72,73]. In a subsequent study [77] the impact of the probe orifice on the predictions was shown to be non-negligible due to passage of gases through the hole instead of a stagnation point at that location and a quantitative correction involving an upstream shift in the numerical sampling location was suggested. The upstream shift as a function of H_p that is used in the present work is summarised in Table 4. An optically thin radiation model is used. Previous work on these flames indicates that including soot radiation tends to overpredict heat loss [12] and to compensate for this soot particle radiation is not considered here. Modelling includes the Soret effect but, based on previous modelling [12] and experimental [78] evidence, the thermophoretic effect is assumed to be small and is not included in the present BSS flame simulations. The 1D mesh is generated automatically by a progressively adaptive procedure [72] and our tests confirm that predictions are insensitive to further mesh refinement.

Table 4
Upstream shift correction for numerical sampling point in 1D BSS simulations.

H_p (mm)	4	4.5	6	8	10	12
Shift (mm)	1.2	1.2	1.4	1.5	1.6	1.6

3.2.2. Results

The temperature profiles with height above the burner for different H_p are shown in the Fig. 4. The predictions show excellent agreement with the experimental measurements. These results justify the optically thin radiation model as discussed above, and demonstrate that the gas-phase chemical kinetics model is satisfactory for this ethylene flame series.

Soot PSD's at the sampling point for different values of H_p are shown in Fig. 5. The predictions are for three values of the coagulation efficiency model parameter, λ. The modelling qualitatively captures the transition from a unimodal PSD for $H_p = .4$ cm through to bimodal shapes for larger values of H_p, but there is strong sensitivity to λ, with a general suppression of the bimodal transition as λ increases, and discrepancies with the data against which the number density of the larger particles is generally overpredicted. Higher values of λ correspond to lower coagulation efficiency and thus a smaller rate of coagulation of smaller particles into larger particles. For $\lambda = 1$ the differences between the predicted and measured PSD's for the smaller stagnation plate separation distances, $H_p = 0.4$ cm and 0.45 cm, appear especially significant. At these relatively small values of H_p the sampled soot is expected to be in an initial stage of evolution where nucleation and initial particle growth are dominant. The rate of coagulation of PAHs into the first BIN species in Rx3 in Table 1 may be too high for $\lambda = 1$. Indeed, much better agreement with the experimental PSD for $H_p = .4$ cm and 0.45 cm is evident when larger values of λ (corresponding to lower coagulation efficiency) are used. Similar shapes of PSD at these two H_p are reported by Veshkini et al. [28] who used a different sectional method that explored the possibility of reversible nucleation and condensation processes. The discrepancy with the data for the smaller values of H_p should also be considered in the context of experimental uncertainty. For $H_p = 0.4$ cm, only a small concentration of particles are measured experimentally with $D < 2.5$ nm which is near the lower detection limit of scanning mobility particle sizers [41]. Furthermore, the soot particles grow rapidly in size from $H_p = 0.4$ cm to 0.45 cm and the PSD is therefore very sensitive to the exact point at which samples are extracted [78].

A pronounced bimodality of the PSD starts to emerge at $H_p = 0.6$ cm as the coagulation of small particles increases relative to their rate of nucleation. Modelling with $\lambda = 1$ and 1.25 qualitatively reproduces the bimodal transition rather well, although the magnitude of the size dependent number density is noticeably larger than the experimental values for all $H_p > 0.6$ cm. As H_p increases from 0.8 cm to 1.2 cm, the nucleation rate diminishes while coagulation continuously consumes small particles to the point that the valley in the bimodal distribution gets deeper. Such evolution of soot particles is accurately captured by $\lambda = 1$ and 1.25 though quantitative overprediction of the number density persists, especially for the larger sized particles. As expected, the modelling with $\lambda = 2$ results in less coagulation of small particles and this is enough to suppress the bimodal transition at $H_p > 0.6$ cm so that the number density of $D < 10$ nm particles is overpredicted while

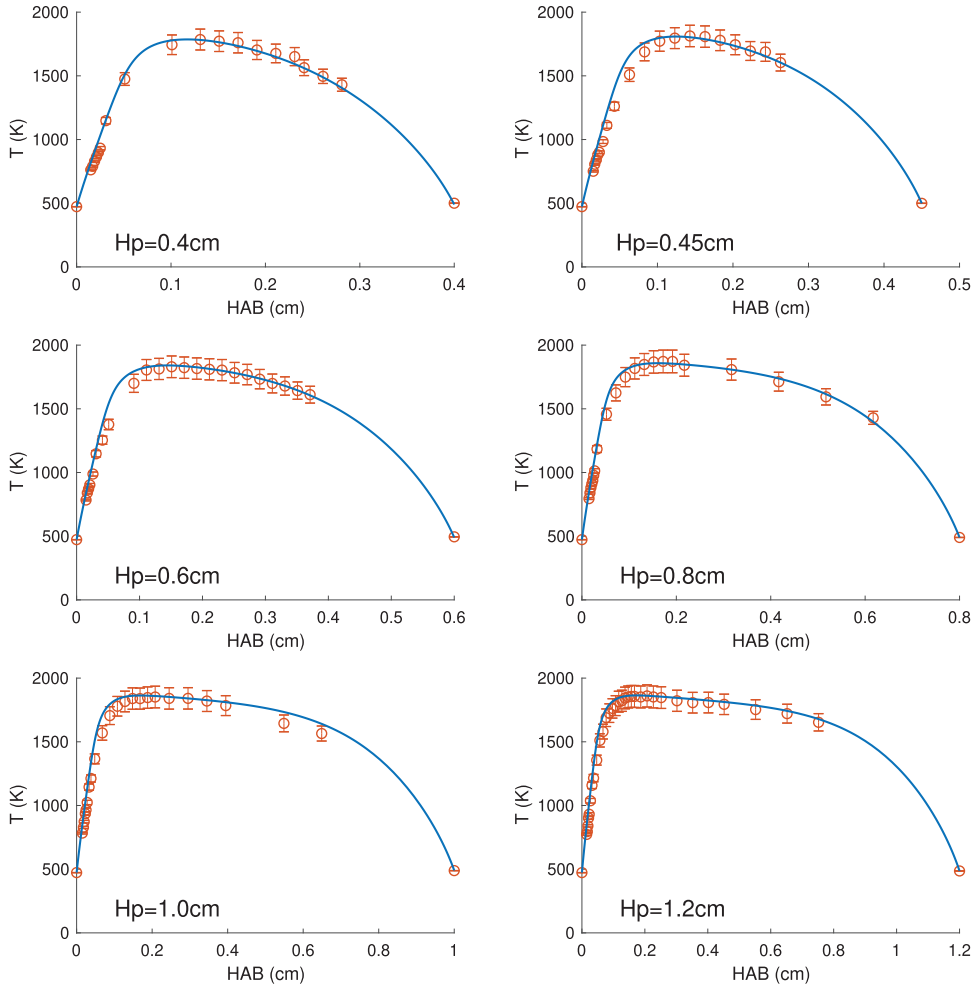

Fig. 4. Temperature profiles in the BSS flames as a function of the height above burner (HAB) for different H_p. Symbols: experimental measurements with error bar [41]; Lines: simulation results.

the predicted larger particle number densities are generally smaller than for $\lambda = 1$ and 1.25.

At this stage, it is difficult know which value of λ best reflects physics. Generally, the results with larger λ, that corresponds to a larger void fraction, gives better agreement to the data for small H_p where the soot particles are less mature and closer in form to nascent soot which may have relatively loosely packed PAH. Conversely, results with smaller λ, that corresponds to smaller void fraction, gives better agreement with the data for cases with larger H_p where the soot is relatively mature and voids are smaller. The results discussed earlier for the coagulation efficiency in Fig. 1 suggest that $\lambda = 2$ works well and results in a coagulation efficiency (and hence coagulation rate if collision frequency is unchanged) that is about an order of magnitude smaller than for $\lambda = 1$. However, $\lambda = 2$ implies a soot particle void fraction of $v_f = 0.5$ which may be too high as it is very close to the critical porosity that causes particle breakup during combustion [79]. The actual soot void fraction will vary with flame conditions, particle history and size due to factors such as internal burning of particles, different PAH stacking arrangements and the possible presence of liquid-like materials within the particles [80]. Therefore we can speculate that λ should be a variable parameter and future work may investigate models for it.

Given the significant uncertainties in the experimental data and in the modelling of soot processes other than coagulation, the development of more sophisticated functions for λ is not attempted at this stage. Nevertheless, in light of the rather good qualitative predictions here and the relatively poor quality of the bimodal soot PSD's that are predicted when simple constant valued [28] and empirical [71] coagulation efficiency models are used, the need for detailed physics-based coagulation models, like the present model, is apparent.

As a point of comparison to the strong sensitivity of the coagulation model to variations in λ, Figure 6 shows the sensitivity of the PSD predictions to the rate of fragmentation described by Rx21 - Rx23 in Table 1. In addition to the base case results where the fragmentation rate coefficients are as reported in the table, results are also shown for no fragmentation (i.e. Rx21–Rx23 are excluded), and for cases where the pre-exponential factors are increased by 10 and 100. All results are for $\lambda = 1$. In contrast to the significant sensitivity of the shape of the PSD to the coagulation rate modelling, the shape and bimodality of the distributions is not significantly affected by variations of fragmentation rate. However, there is significant sensitivity in the number density magnitude at the larger size end of the PSD's for cases with $H_p \leq 0.6$ cm. While any oxidation that takes place in these rich premixed flames is driven by OH, the fragmentation modelled by Rx21 - Rx23 requires the presence of O_2 and the marked difference in the sensitivity for different H_p can be explained by the differences in O_2 mole fractions along the centreline (see Fig. 7). The sensitivity is greatest where the amount of O_2 available at the sampling location is highest (i.e. for $H_p = 0.4$ cm). As the mole fraction of O_2

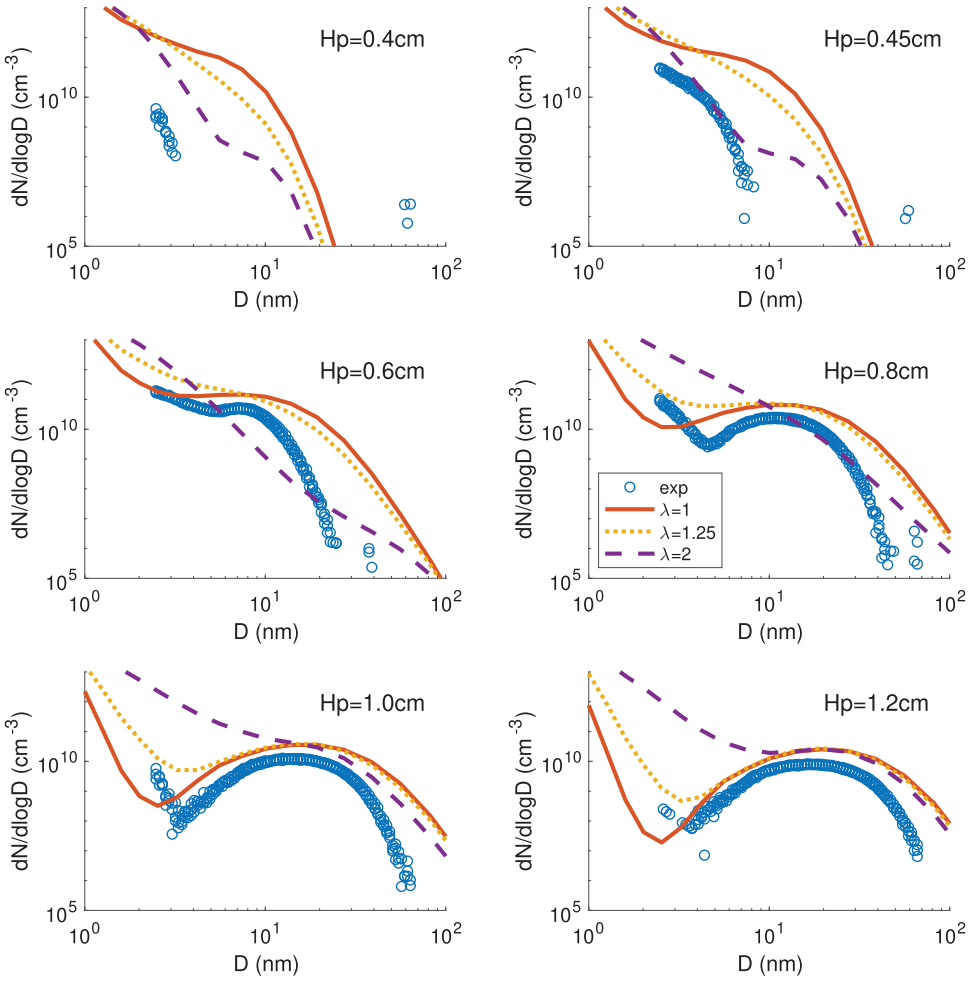

Fig. 5. Soot PSD in the BSS flames for different H_p and λ. Symbols: experimental measurements [41]; Lines: simulation results for different values of λ.

drops the sensitivity of the PSD's to the fragmentation rate coefficients is greatly diminished. Although the results for $H_p \leq 0.6$ with increased fragmentation rate show better agreement to the experimental PSD's, this does not necessarily imply that the standard fragmentation rates shown in Table 1 are too low. It is possible that the coagulation rates are too high and an artificial increase in fragmentation compensates for that error. However, if these significant sensitivities to fragmentation rate are real then the usual assumption that there is negligible fragmentation in rich premixed flames should be qualified by noting that in fact some fragmentation can still occur prior to the full consumption of oxygen.

3.3. Methane laminar coflow diffusion flame

3.3.1. Case setup

The methane laminar coflow diffusion flame burner that was investigated experimentally by Smooke et al. [42] consists of a 12 mm diameter fuel nozzle inside a concentric 102 mm diameter oxidiser coflow tube. The fuel is a mixture of methane (240 cm^3/min) and argon (2.4 cm^3/min) and the oxidiser is air (40,000 cm^3/min). Original data for the soot volume fraction was measured by thermocouple particle densitometry (TPD) and has an estimated absolute uncertainty of 50%. Subsequently Commodo [43] detected soot from this burner setup through a combination of laser induced fluorescence (LIF) and laser induced incandescence (LII). An updated conversion of the measured laser signals to absolute soot volume fraction is reported in Sirignano et al. [10]. Both the Smooke et al. [42] and Sirignano et al. [10] data are used here.

The coflow flame is computed in the 2D axisymmetric OpenSMOKE++ solver [72]. An optically thin radiation model is used and both the Soret and thermophoretic effects are included in the modelling. As was the case for the BSS flames investigated above, soot radiation is omitted to avoid excessive heat loss relative to the data. The computational domain is 160 mm in length and 47.5 mm in width and is discretised by approximately 0.1 million grid cells. The smallest cells in the flame region are about 0.1 mm across and a linear stretch factor is applied outside that region. Our tests confirm that use of a finer mesh does not lead to appreciable differences in the numerical predictions. To account for diffusive preheating of the fuel and air streams the simulation domain is extended 10 mm upstream of the burner exit plane, however conduction through burner walls is not considered.

3.3.2. Results

Figure 8 shows the 2D temperature field overlaid with mixture fraction contour lines along with radial profiles of predicted and experimental temperature at various heights above burner (HAB). The predictions are in excellent agreement with the experimental measurements indicating that the gas-phase chemical kinetics and radiation modelling are suitable for this flame.

Radial profiles of the soot volume fraction for various HAB are shown in Figs. 9–11. Both the TPD and LIF + LII experimental data are included and model predictions are for the same three values of λ that were considered in the analysis of the BSS flames

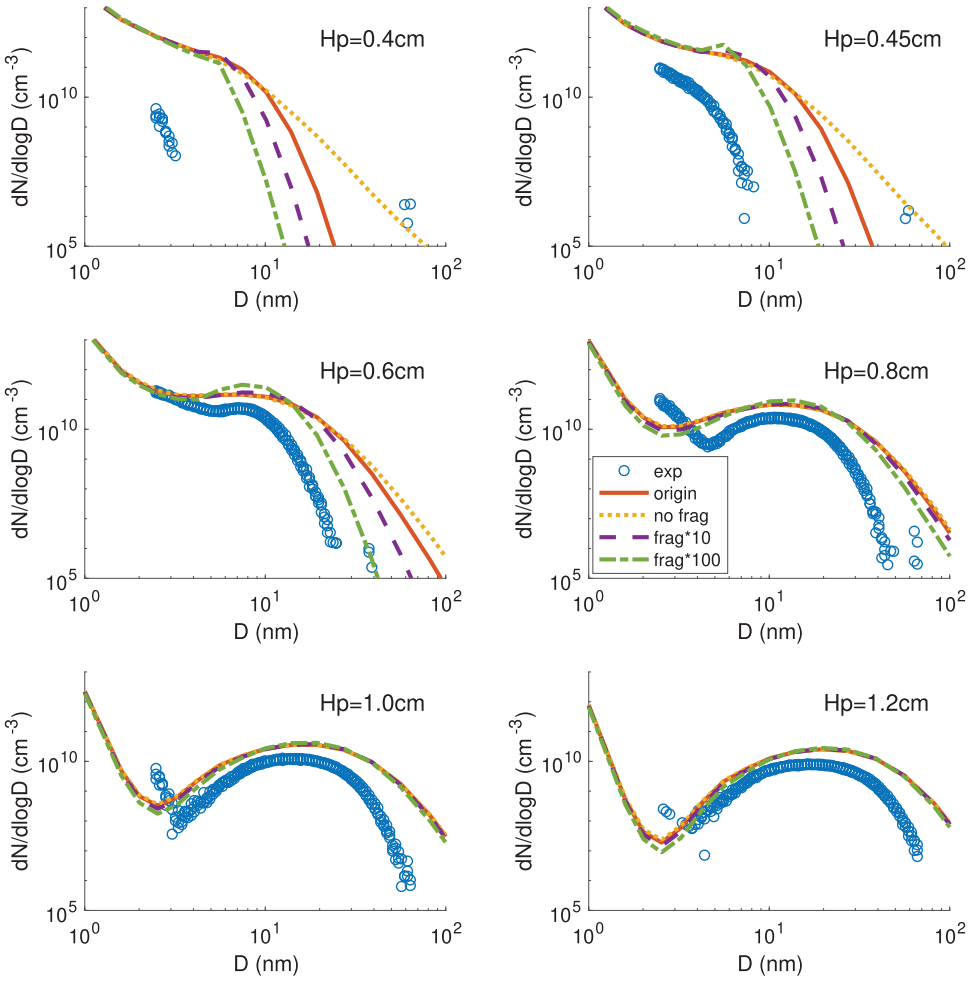

Fig. 6. Soot PSD in the BSS flames for different H_p and fragmentation rates. Symbols: experimental measurements [41]; Lines: simulation results for different values of the pre-exponential factors in Rx21 - Rx23. $\lambda = 1$ is used for all model results.

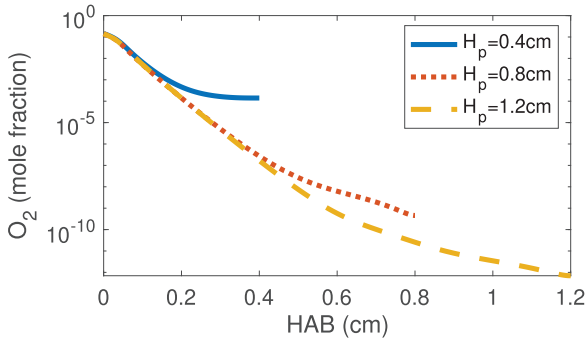

Fig. 7. Centreline profiles of predicted O_2 mole fraction in the BSS flames for different H_p.

above. The predicted soot volume fraction is the summation over the lumped species sections starting from a specified lower numerical detection limit which should match the lower detection limit of the experimental techniques. The lower detection limits of TPD and the laser-based methods are expected to be quite different and, indeed, significant differences between TPD and LIF + LII data are observed at HAB = 20 mm and 25 mm (note that laser-based data was not obtained at the other HAB locations). The TPD data has generally lower magnitude than the LIF + LII data with the former showing almost no soot near the flame axis while the latter indicates appreciable soot along the centreline. Both techniques produce similar peak values in the shear layer although the TPD probe is obtrusive and pushes that peak location to slightly greater radii. The TPD technique relies on the thermophoretic deposition of soot particles onto the sampling probe and the deposition of very small particles, which have low coagulation efficiency, tends to be missed [33]. On the other hand, LIF is able to detect near gaseous molecules and soot particles up to about 4 nm [81]. The lower detection limit of LII is contested. The review by Michelsen [82] refers to evidence of LII signals from particles smaller than 10 nm and Bladh et al. [83] even suggest that LII can probe soot particles as small as 1.5 nm, although this is contradicted by Sirignano et al. [84] who confirmed that nascent soot in the 2–4 nm size range emit LIF but not LII. Although the precise lower experimental detection limits are not known in the present flame case, the soot volume fraction predictions are provided for both a 2 nm lower threshold, which is commensurate with the LIF sensitivity, and a 7 nm lower threshold, which is more appropriate for LII and TPD detection. These numerical limits correspond to bins 5 and 10 in Table 3.

At all HAB there is a consistent reduction in soot volume fraction with increasing λ. For $\lambda = 1$ (Fig. 9) and $\lambda = 1.25$ (Fig. 10), the predicted soot volume fraction profiles have the same shape as the TPD data although the peak value is overpredicted (even for the 7 nm threshold) and the values near the axis generally fall between the TPD and LIF + LII measurements. At HAB = 25 mm the centreline values of the volume fraction are in quite good

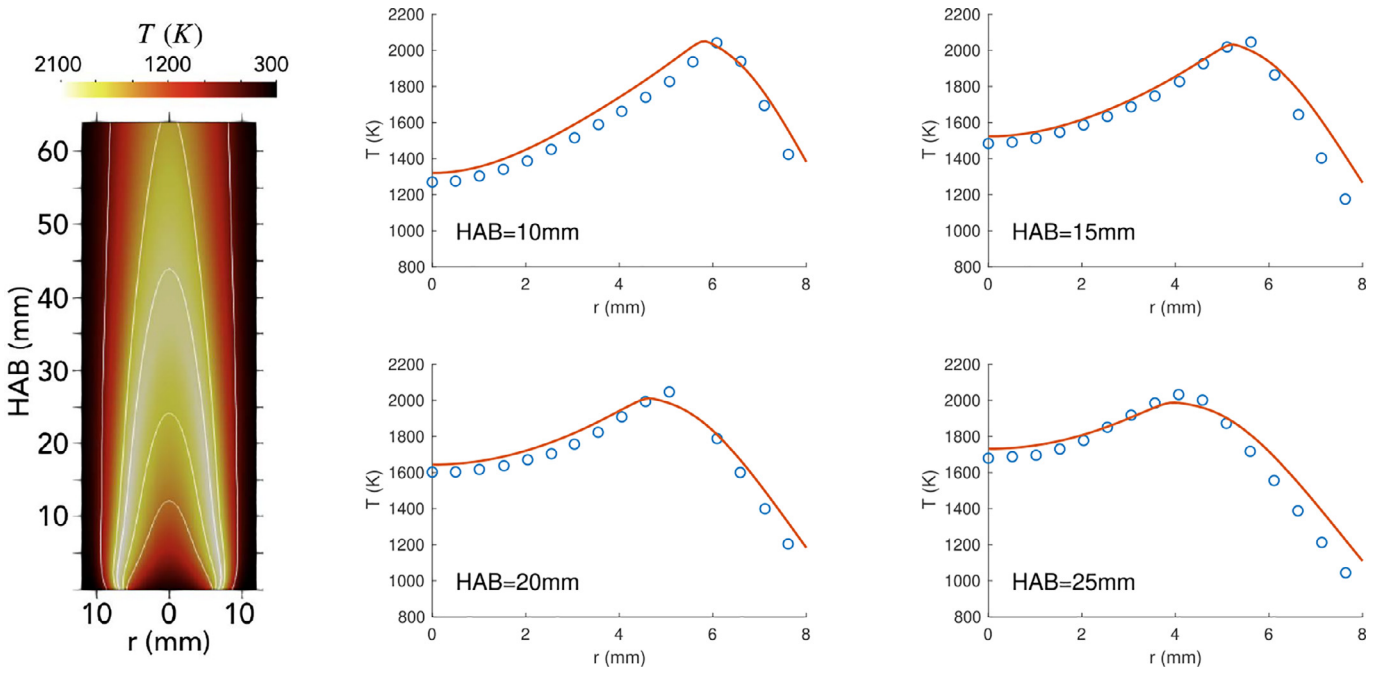

Fig. 8. Temperature field with mixture fraction contour lines from outer to inner of 0.01, 0.04, 0.056, 0.1 and 0.2 (left) and radial profiles of temperature (right) in the methane laminar coflow diffusion flame. Symbols: experimental data [42]; lines: simulation results.

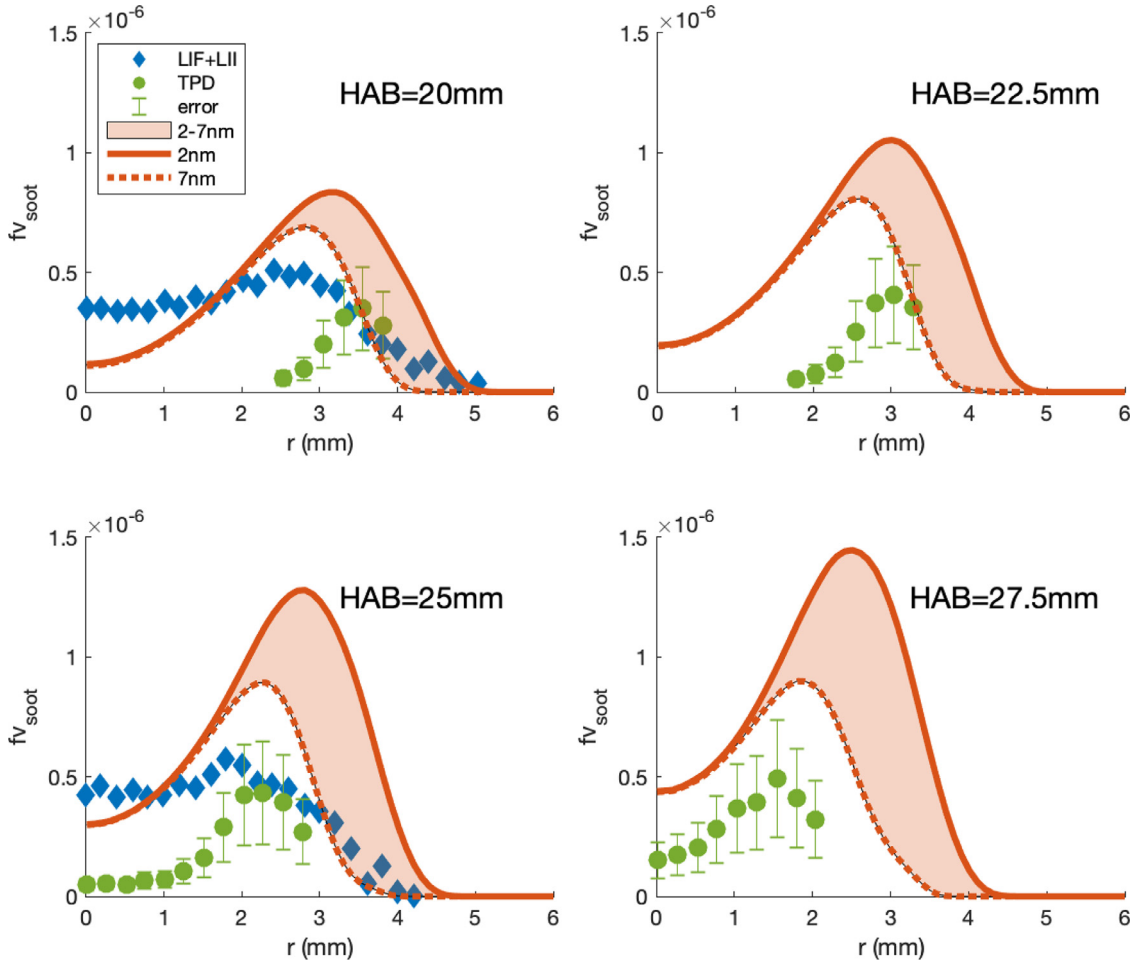

Fig. 9. Radial distributions of soot volume fraction in the methane laminar coflow diffusion flame at different HAB using $\lambda = 1$. Circles: TPD experimental data with error bar [42]; diamonds: LIF and LII experimental data [43]; solid line: numerical detection limit = 2nm; dotted line: numerical detection limit = 7nm; shaded area: soot attributed to particles from 2nm to 7nm.

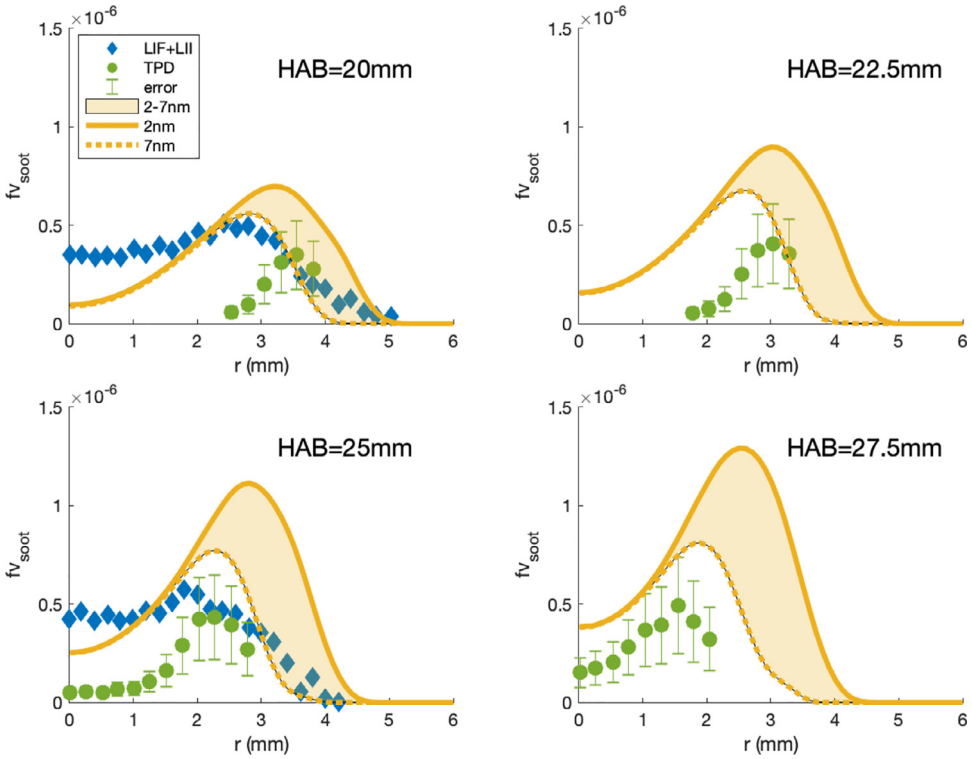

Fig. 10. Radial distributions of soot volume fraction in the methane laminar coflow diffusion flame at different HAB using $\lambda = 1.25$. Circles: TPD experimental data with error bar [42]; diamonds: LIF and LII experimental data [43]; solid line: numerical detection limit = 2nm; dotted line: numerical detection limit = 7nm; shaded area: soot attributed to particles from 2 nm to 7 nm.

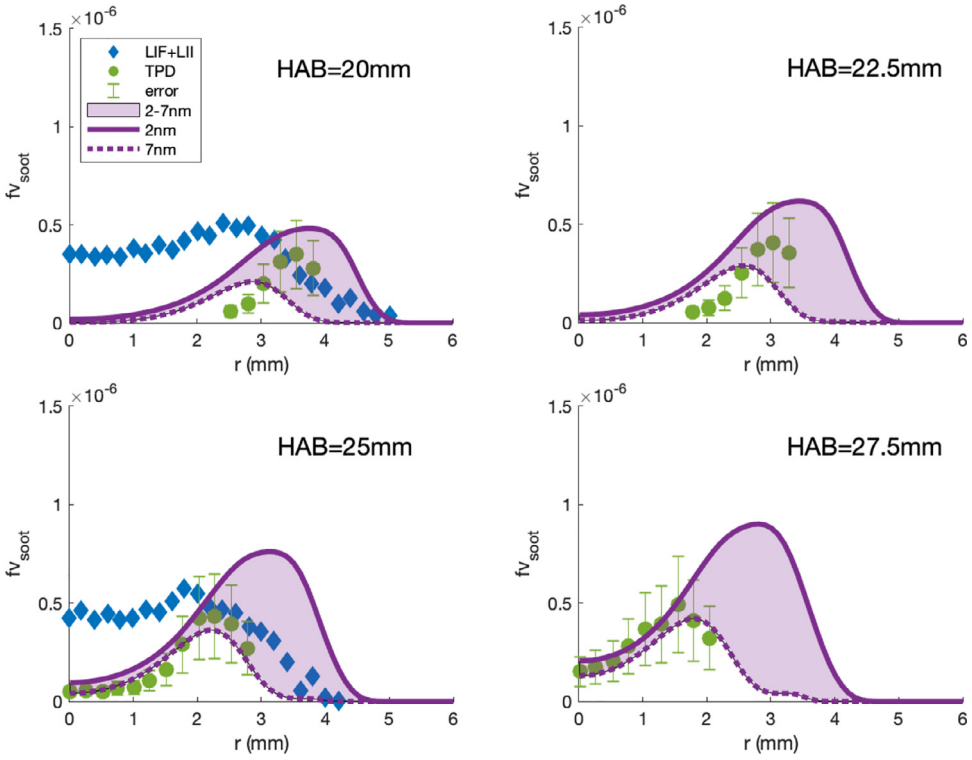

Fig. 11. Radial distributions of soot volume fraction in the methane laminar coflow diffusion flame at different HAB using $\lambda = 2$. Circles: TPD experimental data with error bar [42]; diamonds: LIF and LII experimental data [43]; solid line: numerical detection limit = 2nm; dotted line: numerical detection limit = 7nm; shaded area: soot attributed to particles from 2nm to 7nm.

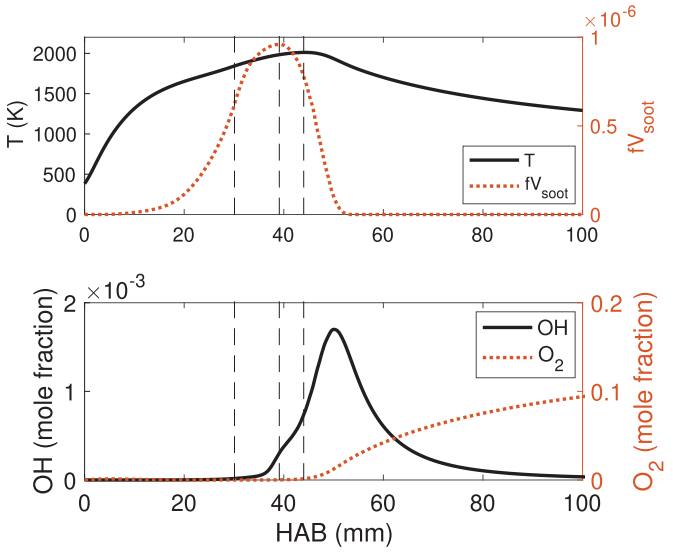

Fig. 12. Centreline profiles of temperature, soot volume fraction, O_2 and *OH* mole fraction in the methane laminar coflow diffusion flame. The vertical dashed lines represent the locations of maximum growth rate of soot, peak soot volume fraction and temperature, respectively.

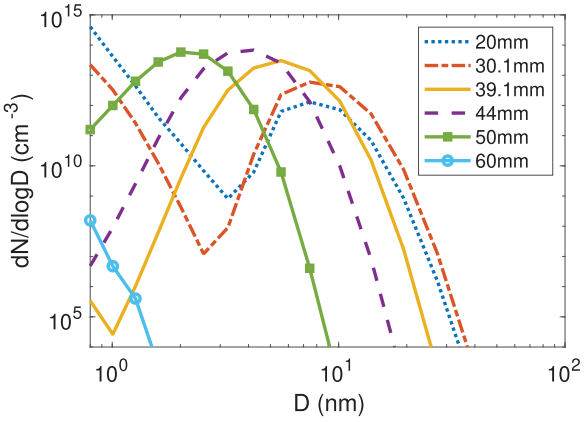

Fig. 13. Evolution of soot PSD in the methane laminar coflow diffusion flame. The legend represents various HAB.

agreement with the LIF + LII data. The $\lambda = 2$ results in Fig. 11 show a remarkable agreement to the TPD data, although we must keep in mind the incorrect PSD shapes for $\lambda = 2$ in the BSS flames. The soot predictions for all λ in the outer shear layer have strong sensitivity to the lower detection limit. In contrast the experimental volume fractions in the outer shear layer are quite similar for both the TPD and LIF + LII techniques. This may be the result of the model yielding a significant concentration of particles within the 2–7 nm size range which happens to correspond to the size range that is not easily detectable in the experiments since it falls outside the typical detection ranges of the combination of measurement methods that were used. Moreover, TPD is strongly affected by oxidation and is known to significantly under measure the soot volume fraction near the flame front [85].

In the absence of experimental soot PSD's, the modelling can provide insight into the soot evolution in the methane laminar coflow diffusion flame. Centreline profiles of temperature, soot volume fraction and mole fractions of O_2 and OH are shown in Fig. 12. Results here are for $\lambda = 1$. The vertical dashed lines at HAB = 30.1 mm, 39.1 mm and 44 mm represent the locations of maximum soot growth rate, peak soot and peak temperature, respectively. It can be seen that soot formation reaches a maximum and starts to decline prior to the peak temperature point after which there is increasing amounts of oxidants available and rapid soot burn out. Predicted soot PSD's at various HAB are shown in Fig. 13. At HAB = 20 mm the soot volume fraction is just starting to rise steeply, but the PSD already exhibits a mature bimodal distribution. As the soot particles are convected downstream to HAB = 30.1 mm where the soot growth rate reach its maximum, there is an increase of the number density of larger sized particles while there is rather strong consumption of particles smaller than around 4 nm by coagulation. At HAB = 39.1 mm, where soot volume fraction peaks and growth rate equals oxidation rate, it is found that the largest soot particles have begun to fragment and the small particles are mostly depleted due to oxidation with the increasing concentration of both O_2 and OH. This results in an accumulation of medium-sized particles in the 2–10 nm range. At HAB = 44mm where the centreline temperature reaches a maximum, the soot PSD has reverted to a unimodal shape. The number density of large sized particles has reduced significantly and there is an increased concentration of small soot particles. This trend is even more pronounced at HAB = 50 mm and 60 mm. This increased presence of small particles is not due to nucleation but rather they are the fragmented pieces of formerly large soot particles. This may imply that fragmentation into smaller particles is occurring faster than those small particles can be consumed by oxidation, supporting a view that soot burnout is initiated by fragmentation which provides higher soot surface area on which subsequent oxidation can take place.

4. Conclusion

This paper has presented a novel coagulation efficiency model based on the thermal rebound concept in which colliding soot particles coagulate if they have insufficient thermal kinetic energy to escape the interaction potential well. Here, the interaction potential well depth is based on a minimisation of the Lennard-Jones potential and accounts for the interaction of spherical particles with explicit dependence on size and material composition. In principle, the new coagulation efficiency model is also applicable to other soot modelling approaches including the method of moments although in that approach there would need to be integration of the coagulation efficiency across all particle sizes, and once again the fitted Arrhenius-like formulation that has been presented in this work could potentially ease the numerical implementation. A model parameter λ, that is related to the soot particle void fraction, was taken as a constant in the present work and sensitivity of predictions for λ between 1 and 2 was investigated. The coagulation model has been combined with a sectional soot kinetics scheme with discretisation in particle size space and has been validated by comparison to experimental data for a series of burner stabilised stagnation (BSS) ethylene flames and a methane laminar coflow diffusion flame.

The following conclusions are made:

- The numerical predictions in both flame configurations show overall good agreement to experimental data, but strong sensitivity to the parameter λ has been found. In addition the comparison of the predicted soot volume fraction to experimental data is dependent on the lower detection limit which defines the smallest detectable size of soot particles, and here both 2 nm and 7 nm thresholds were used.
- In the BSS simulations, the transition from a unimodal PSD at smaller stagnation plate separation distances to a bimodal PSD at larger separation distances is captured very well for modelling with $\lambda = 1$ and 1.25, but there is an overprediction of the number density at the larger particle size end of the dis-

tribution. For $\lambda = 2$, corresponding to a void fraction of 0.5, the coagulation rate is much lower and the PSD for smaller separation distances is quite well predicted but the transition to a bimodal distribution is suppressed. It is very unlikely that λ is a constant and future research may focus on this topic.

- In the methane coflow diffusion flame simulations, as λ is increased the soot volume fraction reduces noticeably. Agreement with the LIF + LII data near the flame axis is quite good for $\lambda = 1$ and 1.25 but there is general overprediction of soot volume fraction in the shear layer. For $\lambda = 2$ there is better agreement to the data in the shear layer. The predictions in the shear layer also have a strong sensitivity to the lower detection limit. This is in contrast to the experimental data in the shear layer which is similar for all measurement techniques, perhaps due to the large number of particles in the 2–7 nm range which is not easy to detect using LIF, LII or TPD.

Declaration of Competing Interest

The authors declare that they have no known competing financial interests or personal relationships that could have appeared to influence the work reported in this paper.

Acknowledgments

The research was supported by the Australian Research Council under grant number DP180104190. Computational resources in this work are provided by Intersect.org.au through a merit allocation scheme and the high-performance computing facility at the University of Sydney, Artemis. We are grateful to Prof. J.H. Kent from the University of Sydney and Prof. A. D'Anna from the University of Naples Federico II for provision of code and data associated with the sectional kinetics scheme.

Supplementary material

Supplementary material associated with this article can be found, in the online version, at doi:10.1016/j.combustflame.2021.111444.

References

[1] A. Kazakov, M. Frenklach, Dynamic modeling of soot particle coagulation and aggregation: implementation with the method of moments and application to high-pressure laminar premixed flames, Combust. Flame 114 (1998) 484–501.
[2] M. Frenklach, Method of moments with interpolative closure, Chem. Eng. Sci. 57 (2002) 2229–2239.
[3] D.L. Marchisio, R.O. Fox, Solution of population balance equations using the direct quadrature method of moments, J. Aerosol Sci. 36 (2005) 43–73.
[4] M.E. Mueller, G. Blanquart, H. Pitsch, Hybrid method of moments for modeling soot formation and growth, Combust. Flame 156 (2009) 1143–1155.
[5] M. Balthasar, M. Kraft, A stochastic approach to calculate the particle size distribution function of soot particles in laminar premixed flames, Combust. Flame 133 (2003) 289–298.
[6] A. Violi, Modeling of soot particle inception in aromatic and aliphatic premixed flames, Combust. Flame 139 (2004) 279–287.
[7] S. Kumar, D. Ramkrishna, On the solution of population balance equations by discretization: III. Nucleation, growth and aggregation of particles, Chem. Eng. Sci. 52 (1997) 4659–4679.
[8] S. Rigopoulos, Population balance modelling of polydispersed particles in reactive flows, Prog. Energy Combust. Sci. 36 (2010) 412–443.
[9] R.P. Lindstedt, B.B.O. Waldheim, Modeling of soot particle size distributions in premixed stagnation flow flames, Proc. Combust. Inst. 34 (2013) 1861–1868.
[10] M. Sirignano, J. Kent, A. D'Anna, Modeling formation and oxidation of soot in nonpremixed flames, Energy Fuels 27 (2013) 2303–2315.
[11] M. Sirignano, J. Kent, A. D'Anna, Detailed modeling of size distribution functions and hydrogen content in combustion-formed particles, Combust. Flame 157 (2010) 1211–1219.
[12] C. Saggese, S. Ferrario, J. Camacho, A. Cuoci, A. Frassoldati, E. Ranzi, H. Wang, T. Faravelli, Kinetic modeling of particle size distribution of soot in a premixed burner-stabilized stagnation ethylene flame, Combust. Flame 162 (2015) 3356–3369.
[13] J. Appel, H. Bockhorn, M. Frenklach, Kinetic modeling of soot formation with detailed chemistry and physics: laminar premixed flames of C2 hydrocarbons, Combust. Flame 121 (2000) 122–136.
[14] H. Richter, S. Granata, W.H. Green, J.B. Howard, Detailed modeling of PAH and SOOT formation in a laminar premixed benzene/oxygen/argon low-pressure flame, Proc. Combust. Inst. 30 (2005) 1397–1405.
[15] A. D'Anna, J.H. Kent, Modeling of particulate carbon and species formation in coflowing diffusion flames of ethylene, Combust. Flame 144 (2006) 249–260.
[16] A. D'anna, J.H. Kent, A model of particulate and species formation applied to laminar, nonpremixed flames for three aliphatic-hydrocarbon fuels, Combust. Flame 152 (2008) 573–587.
[17] M. Sirignano, J. Kent, A. D'Anna, Further experimental and modelling evidences of soot fragmentation in flames, Proc. Combust. Inst. 35 (2015) 1779–1786.
[18] H. Richter, J.B. Howard, Formation of polycyclic aromatic hydrocarbons and their growth to soot: a review of chemical reaction pathways, Prog. Energy Combust. Sci. 26 (2000) 565–608.
[19] M. Frenklach, Reaction mechanism of soot formation in flames, Phys. Chem. Chem. Phys. 4 (2002) 2028–2037.
[20] M. Frenklach, A.M. Mebel, On the mechanism of soot nucleation, Phys. Chem. Chem. Phys. 22 (2020) 5314–5331.
[21] M. Frenklach, H. Wang, Detailed modeling of soot particle nucleation and growth, Symp. (Int.) Combust. 23 (1991) 1559–1566.
[22] H. Bockhorn, Soot Formation in Combustion: Mechanisms and Models, volume 59, Springer Science & Business Media, 2013.
[23] S.K. Friedlander, Smoke, Dust, and Haze, Oxford University Press, New York, 2000.
[24] K.G. Neoh, J.B. Howard, A.F. Sarofim, Effect of oxidation on the physical structure of soot, Symp. (Int.) Combust. 20 (1985) 951–957.
[25] C.A. Echavarria, I.C. Jaramillo, A.F. Sarofim, J.S. Lighty, Studies of soot oxidation and fragmentation in a two-stage burner under fuel-lean and fuel-rich conditions, Proc. Combust. Inst. 33 (2011) 659–666.
[26] M.E. Mueller, G. Blanquart, H. Pitsch, Modeling the oxidation-induced fragmentation of soot aggregates in laminar flames, Proc. Combust. Inst. 33 (2011) 667–674.
[27] A. Liu, S. Rigopoulos, A conservative method for numerical solution of the population balance equation, and application to soot formation, Combust. Flame 205 (2019) 506–521.
[28] A. Veshkini, N.A. Eaves, S.B. Dworkin, M.J. Thomson, Application of PAH-condensation reversibility in modeling soot growth in laminar premixed and nonpremixed flames, Combust. Flame 167 (2016) 335–352.
[29] L. Tian, M.A. Schiener, R.P. Lindstedt, Fully coupled sectional modelling of soot particle dynamics in a turbulent diffusion flame, Proc. Combust. Inst. (2020).
[30] D. Hou, D. Zong, C.S. Lindberg, M. Kraft, X. You, On the coagulation efficiency of carbonaceous nanoparticles, J. Aerosol Sci. 140 (2020) 105478.
[31] J.H. Seinfeld, S.N. Pandis, Atmospheric Chemistry and Physics: From Air Pollution to Climate Change, John Wiley & Sons, 2016.
[32] B. Zhao, Z. Yang, M.V. Johnston, H. Wang, A.S. Wexler, M. Balthasar, M. Kraft, Measurement and numerical simulation of soot particle size distribution functions in a laminar premixed ethylene-oxygen-argon flame, Combust. Flame 133 (2003) 173–188.
[33] A. D'Alessio, A.C. Barone, R. Cau, A. D'Anna, P. Minutolo, Surface deposition and coagulation efficiency of combustion generated nanoparticles in the size range from 1 to 10 nm, Proc. Combust. Inst. 30 (2005) 2595–2603.
[34] M. Sirignano, A. D'Anna, Coagulation of combustion generated nanoparticles in low and intermediate temperature regimes: an experimental study, Proc. Combust. Inst. 34 (2013) 1877–1884.
[35] J. Singh, R.I.A. Patterson, M. Kraft, H. Wang, Numerical simulation and sensitivity analysis of detailed soot particle size distribution in laminar premixed ethylene flames, Combust. Flame 145 (2006) 117–127.
[36] C. Eberle, P. Gerlinger, M. Aigner, A sectional PAH model with reversible PAH chemistry for CFD soot simulations, Combust. Flame 179 (2017) 63–73.
[37] Q. Zhang, H. Guo, F. Liu, G. Smallwood, M. Thomson, Modeling of soot aggregate formation and size distribution in a laminar ethylene/air coflow diffusion flame with detailed PAH chemistry and an advanced sectional aerosol dynamics model, Proc. Combust. Inst. 32 (2009) 761–768.
[38] A. Raj, M. Sander, V. Janardhanan, M. Kraft, A study on the coagulation of polycyclic aromatic hydrocarbon clusters to determine their collision efficiency, Combust. Flame 157 (2010) 523–534.
[39] H. Wang, G. Kasper, Filtration efficiency of nanometer-size aerosol particles, J. Aerosol Sci. 22 (1991) 31–41.
[40] H.C. Hamaker, The London-Van der Waals attraction between spherical particles, Physica 4 (1937) 1058–1072.
[41] A.D. Abid, J. Camacho, D.A. Sheen, H. Wang, Quantitative measurement of soot particle size distribution in premixed flames–the burner-stabilized stagnation flame approach, Combust. Flame 156 (2009) 1862–1870.
[42] M.D. Smooke, C.S. McEnally, L.D. Pfefferle, R.J. Hall, M.B. Colket, Computational and experimental study of soot formation in a coflow, laminar diffusion flame, Combust. Flame 117 (1999) 117–139.
[43] M. Commodo, Diagnostic for the Characterization of Nanometric Structures in High Temperature Reactive Systems, Ph. D. Thesis, University of Napoli Federico II, 2007 Ph.D. thesis.
[44] A. D'Anna, M. Sirignano, J. Kent, A model of particle nucleation in premixed ethylene flames, Combust. Flame 157 (2010) 2106–2115.
[45] G. P. Smith, D. M. Golden, M. Frenklach, N. W. Moriarty, B. Eiteneer, M. Goldenberg, C. T. Bowman, R. K. Hanson, S. Song, W. C. Gardiner Jr, et al., The gri 3.0 chemical kinetic mechanism, Gas Research Institute, Chicago, IL, http://www.me. berkeley. edu/gri_mech (1999). http://www.me.berkeley.edu/gri_mech.

[46] J.A. Miller, C.F. Melius, Kinetic and thermodynamic issues in the formation of aromatic compounds in flames of aliphatic fuels, Combust. Flame 91 (1992) 21–39.
[47] N.M. Marinov, W.J. Pitz, C.K. Westbrook, M.J. Castaldi, S.M. Senkan, Modeling of aromatic and polycyclic aromatic hydrocarbon formation in premixed methane and ethane flames, Combust. Sci. Technol. 116 (1996) 211–287.
[48] A. D'Anna, A. Violi, A kinetic model for the formation of aromatic hydrocarbons in premixed laminar flames, Symp. (Int.) Combust. 27 (1998) 425–433.
[49] W. Pejpichestakul, E. Ranzi, M. Pelucchi, A. Frassoldati, A. Cuoci, A. Parente, T. Faravelli, Examination of a soot model in premixed laminar flames at fuel-rich conditions, Proc. Combust. Inst. 37 (1) (2019) 1013–1021.
[50] E. Ranzi, C. Cavallotti, A. Cuoci, A. Frassoldati, M. Pelucchi, T. Faravelli, New reaction classes in the kinetic modeling of low temperature oxidation of n-alkanes, Combust. Flame 162 (5) (2015) 1679–1691.
[51] J. Park, S. Burova, A. Rodgers, M.-C. Lin, Experimental and theoretical studies of the c6h5+ c6h6 reaction, J. Phys. Chem. A 103 (1999) 9036–9041.
[52] J. Park, M.-C. Lin, Kinetics for the recombination of phenyl radicals, J. Phys. Chem. A 101 (1997) 14–18.
[53] M. Frenklach, H. Wang, Detailed Mechanism and Modeling of Soot Particle Formation, Springer, 1994.
[54] F. Xu, A.M. El-Leathy, C.H. Kim, G.M. Faeth, Soot surface oxidation in hydrocarbon/air diffusion flames at atmospheric pressure, Combust. Flame 132 (2003) 43–57.
[55] E. Cunningham, On the velocity of steady fall of spherical particles through fluid medium, Proc. R. Soc. Lond. 83 (1910) 357–365.
[56] C.N. Davies, Definitive equations for the fluid resistance of spheres, Proc. Phys. Soc. 57 (1945) 259.
[57] E. Otto, H. Fissan, S. Park, K. Lee, The log-normal size distribution theory of Brownian aerosol coagulation for the entire particle size range: part II - analytical solution using dahneke's coagulation kernel, J. Aerosol. Sci. 30 (1) (1999) 17–34.
[58] D.A. McQuarrie, J.D. Simon, Physical Chemistry: a Molecular Approach, Sterling Publishing Company, 1997.
[59] G. Narsimhan, E. Ruckenstein, The Brownian coagulation of aerosols over the entire range of Knudsen numbers: connection between the sticking probability and the interaction forces, J. Colloid Interface Sci. 104 (1985) 344–369.
[60] R.A. Svehla, Estimated Viscosities and Thermal Conductivities of Gases at High Temperatures, NASA Technical Report R-132, 1963.
[61] C.L. Kong, Combining rules for intermolecular potential parameters. II. Rules for the Lennard-Jones (12-6) potential and the morse potential, J. Chem. Phys. 59 (1973) 2464–2467.
[62] M. Rapacioli, F. Calvo, F. Spiegelman, C. Joblin, D. Wales, Stacked clusters of polycyclic aromatic hydrocarbon molecules, J. Phys. Chem. A 109 (2005) 2487–2497.
[63] L. Pascazio, M. Sirignano, A. D'Anna, Simulating the morphology of clusters of polycyclic aromatic hydrocarbons: the influence of the intermolecular potential, Combust. Flame 185 (2017) 53–62.
[64] M.S. Celnik, M. Sander, A. Raj, R.H. West, M. Kraft, Modelling soot formation in a premixed flame using an aromatic-site soot model and an improved oxidation rate, Proc. Combust. Inst. 32 (2009) 639–646.
[65] G. Blanquart, H. Pitsch, Analyzing the effects of temperature on soot formation with a joint volume-surface-hydrogen model, Combust. Flame 156 (2009) 1614–1626.
[66] R.J. Kee, G. Dixon-Lewis, J. Warnatz, M.E. Coltrin, J.A. Miller, A Fortran Computer Code Package for the Evaluation of Gas-phase Multicomponent Transport Properties, Report No. SAND86-8246, Sandia National Laboratories, Livermore, CA, USA, 1986.
[67] O.A. von Lilienfeld, D. Andrienko, Coarse-grained interaction potentials for polyaromatic hydrocarbons, J. Chem. Phys. 124 (2006) 054307.
[68] A. Bondi, Van der waals volumes and radii, J. Phys. Chem. 68 (1964) 441–451.
[69] G.W. Stewart, Diffraction of x-rays in liquids: benzene, cyclohexane and certain of their derivatives, Phys. Rev. 33 (1929) 889.
[70] T. Blacha, M. Di Domenico, P. Gerlinger, M. Aigner, Soot predictions in premixed and non-premixed laminar flames using a sectional approach for PAHs and soot, Combust. Flame 159 (1) (2012) 181–193.
[71] C. Saggese, N.E. Snchez, A. Frassoldati, A. Cuoci, T. Faravelli, M.U. Alzueta, E. Ranzi, Kinetic modeling study of polycyclic aromatic hydrocarbons and soot formation in acetylene pyrolysis, Energy Fuels 28 (2014) 1489–1501.
[72] A. Cuoci, A. Frassoldati, T. Faravelli, E. Ranzi, Numerical modeling of laminar flames with detailed kinetics based on the operator-splitting method, Energy Fuels 27 (2013) 7730–7753.
[73] A. Cuoci, A. Frassoldati, T. Faravelli, E. Ranzi, Opensmoke++: an object-oriented framework for the numerical modeling of reactive systems with detailed kinetic mechanisms, Comput. Phys. Commun. 192 (2015) 237–264.
[74] H.G. Weller, G. Tabor, H. Jasak, C. Fureby, A tensorial approach to computational continuum mechanics using object-oriented techniques, Comput. Phys. 12 (1998) 620–631.
[75] Q. Song, B. He, Q. Yao, Z. Meng, C. Chen, Influence of diffusion on thermogravimetric analysis of carbon black oxidation, Energy Fuels 20 (5) (2006) 1895–1900.
[76] H. Ghiassi, P. Toth, I.C. Jaramillo, J.S. Lighty, Soot oxidation-induced fragmentation: part 1: the relationship between soot nanostructure and oxidation-induced fragmentation, Combust. Flame 163 (2016) 179–187.
[77] C. Saggese, A. Cuoci, A. Frassoldati, S. Ferrario, J. Camacho, H. Wang, T. Faravelli, Probe effects in soot sampling from a burner-stabilized stagnation flame, Combust. Flame 167 (2016) 184–197.
[78] J. Camacho, C. Liu, C. Gu, H. Lin, Z. Huang, Q. Tang, X. You, C. Saggese, Y. Li, H. Jung, et al., Mobility size and mass of nascent soot particles in a benchmark premixed ethylene flame, Combust. Flame 162 (2015) 3810–3822.
[79] A.R. Kerstein, S. Niksa, Fragmentation during carbon conversion: predictions and measurements, Symp. (Int.) Combust. 20 (1985) 941–949.
[80] A.D. Abid, N. Heinz, E.D. Tolmachoff, D.J. Phares, C.S. Campbell, H. Wang, On evolution of particle size distribution functions of incipient soot in premixed ethylene–oxygen–argon flames, Combust. Flame 154 (4) (2008) 775–788.
[81] M. Conturso, M. Sirignano, A. D'Anna, Effect of alkylated aromatics on particle formation in diffusion flames: an experimental study, Exp. Therm. Fluid Sci. 73 (2016) 27–32.
[82] H.A. Michelsen, Probing soot formation, chemical and physical evolution, and oxidation: a review of in situ diagnostic techniques and needs, Proc. Combust. Inst. 36 (2017) 717–735.
[83] H. Bladh, N.-E. Olofsson, T. Mouton, J. Simonsson, X. Mercier, A. Faccinetto, P.-E. Bengtsson, P. Desgroux, Probing the smallest soot particles in low-sooting premixed flames using laser-induced incandescence, Proc. Combust. Inst. 35 (2015) 1843–1850.
[84] M. Sirignano, D. Bartos, M. Conturso, M. Dunn, A. D'Anna, A.R. Masri, Detection of nanostructures and soot in laminar premixed flames, Combust. Flame 176 (2017) 299–308.
[85] G. De Falco, M. Sirignano, M. Commodo, L. Merotto, F. Migliorini, R. Dondè, S. De Iuliis, P. Minutolo, A. D'Anna, Experimental and numerical study of soot formation and evolution in co-flow laminar partially premixed flames, Fuel 220 (2018) 396–402.